1-1-2013

The SLUGGS survey: the globular cluster systems of three early-type galaxies using wide-field imaging

S. S. Kartha
Swinburne University

D. A. Forbes
Swinburne University

L. R. Spitler
Macquarie University

Aaron J. Romanowsky
San Jose State University, aaron.romanowsky@sjsu.edu

J. A. Arnold
University of California Observatories

See next page for additional authors

Recommended Citation

S. S. Kartha, D. A. Forbes, L. R. Spitler, Aaron J. Romanowsky, J. A. Arnold, and J. P. Brodie. "The SLUGGS survey: the globular cluster systems of three early-type galaxies using wide-field imaging" *Monthly Notices of the Royal Astronomical Society* (2013). https://doi.org/10.1093/mnras/stt1880

Authors

S. S. Kartha, D. A. Forbes, L. R. Spitler, Aaron J. Romanowsky, J. A. Arnold, and J. P. Brodie

Monthly Notices
of the
ROYAL ASTRONOMICAL SOCIETY

MNRAS **437,** 273–292 (2014) doi:10.1093/mnras/stt1880
Advance Access publication 2013 November 14

The SLUGGS survey*: the globular cluster systems of three early-type galaxies using wide-field imaging

Sreeja S. Kartha,[1]† Duncan A. Forbes,[1]† Lee R. Spitler,[1,2,3] Aaron J. Romanowsky,[4,5]
Jacob A. Arnold[5] and Jean P. Brodie[5]

[1] *Centre for Astrophysics & Supercomputing, Swinburne University, Hawthorn VIC 3122, Australia*
[2] *Macquarie University, Macquarie Park, Sydney, NSW 2113, Australia*
[3] *Australian Astronomical Observatory, PO Box 915, North Ryde, NSW 1670, Australia*
[4] *Department of Physics and Astronomy, San José State University, One Washington Square, San Jose, CA 95192, USA*
[5] *University of California Observatories, 1156 High St., Santa Cruz, CA 95064, USA*

Accepted 2013 October 2. Received 2013 October 2; in original form 2013 July 2

ABSTRACT

We present the results from a wide-field imaging study of globular cluster (GC) systems in three early-type galaxies. Combinations of Subaru/Suprime-Cam, Canada–France–Hawaii Telescope/MegaCam and *Hubble Space Telescope*/Wide Field Planetary Camera 2/Advanced Camera for Surveys data were used to determine the GC system properties of three highly flattened galaxies NGC 720, NGC 1023 and NGC 2768. This work is the first investigation of the GC system in NGC 720 and NGC 2768 to very large galactocentric radius (∼100 kpc). The three galaxies have clear blue and red GC subpopulations. The radial surface densities of the GC systems are fitted with Sérsic profiles, and detected out to 15, 8 and 10 galaxy effective radii, respectively. The total number of GCs and specific frequency are determined for each GC system. The ellipticity of the red subpopulation is in better agreement with the host galaxy properties than is the blue subpopulation, supporting the traditional view that metal-rich GCs are closely associated with the bulk of their host galaxies' field stars, while metal-poor GCs reflect a distinct stellar halo. With the addition of another 37 literature studied galaxies, we present a new correlation of GC system extent with host galaxy effective radius. We find a dependence of the relative fraction of blue to red GCs on host galaxy environmental density for lenticular galaxies (but not for elliptical or spiral galaxies). We propose that tidal interactions between galaxies in cluster environments might be the reason behind the observed trend for lenticular galaxies.

Key words: galaxies: elliptical and lenticular, cD – galaxies: individual: NGC 720 – galaxies: individual: NGC 1023 – galaxies: individual: NGC 2768 – galaxies: star clusters: general.

1 INTRODUCTION

Globular clusters (GCs) are present in almost all large galaxies and are good tracers of host galaxy properties (Brodie & Strader 2006). They are very compact objects and thus able to withstand the powerful events of galaxy evolution. They are expected to form during the initial proto-galactic collapse and in gas-rich merging events; as a consequence they trace the field stars that form along with them (Brodie & Huchra 1991; Forbes et al. 1996; Côté, Marzke & West 1998). The luminosity and compact size of GCs make them the brightest and most easily identifiable individual objects out to large (∼200 kpc) galactocentric radii around galaxies (Spitler et al. 2012). This makes them a convenient probe to study galaxy formation at large radii where the surface brightness of the host galaxy stars rapidly drops with increasing radius.

GC systems can be studied using accurate photometry, from which a bimodal nature of the colour distribution is identified (Ashman & Zepf 1992; Forbes, Brodie & Grillmair 1997; Kundu & Whitmore 2001; Peng et al. 2006; Harris 2009a; Sinnott et al. 2010; Liu et al. 2011). Bimodality indicates two subpopulations in a galaxy (Brodie et al. 2012). In some cases, the colour distribution is even found to be trimodal, e.g. in the case of NGC 4365 (Blom, Spitler & Forbes 2012) and NGC 4382 (Peng et al. 2006). The components of the bimodal colour distributions are identified in terms of metallicity: metal rich and metal poor corresponding to red and blue subpopulations, respectively (Usher et al. 2012). The presence of these subpopulations indicates that there were multiple episodes of star formation and metal enrichment in the past.

---

* http://sluggs.swin.edu.au/

† E-mail: skartha@astro.swin.edu.au (SSK); dforbes@astro.swin.edu.au (DAF)

Published by Oxford University Press on behalf of the Royal Astronomical Society

To explain the bimodality in the colour distribution in the context of host galaxy formation, three broad scenarios have been put forward. Ashman & Zepf (1992) proposed that the colour bimodality is the result of a gas-rich merger of disc galaxies. They suggested that the blue GCs are intrinsic to the spiral galaxies, while red GCs are formed during the merger. Forbes et al. (1997) suggested an in situ formation scenario, in which the blue GCs are formed first in the initial collapse with limited field star formation. A quiescent period follows, and then red GCs are formed in a metal-rich environment along with the bulk of the stars in the galaxy. Accretion of blue GCs may also contribute. A third scenario was proposed by Côté et al. (1998, 2000) and Côté, West & Marzke (2002) in which the red GCs are inherent to the host galaxy (similar to Forbes et al. 1997), while the blue GCs are accreted via mergers or tidal stripping. Signatures of these different stages of galaxy evolution are best preserved in galaxy outer haloes rather than in the complex inner regions, and hence, an investigation of GCs in outer haloes gives a unique opportunity to trace the formation and evolution of host galaxies.

In this paper, we present the results from a wide-field imaging study of GC systems in three early-type galaxies: NGC 720 (E5), NGC 1023 (S0) and NGC 2768 (E/S0). A more detailed discussion about individual galaxy characteristics is given in Section 1.1. The data presented in this paper are a part of an ongoing larger survey, the SAGES Legacy Unifying Globulars and GalaxieS (SLUGGS),[1] which aims to understand the assembly history of early-type galaxies with the aid of imaging, spectroscopy and simulations of galaxy formation. The survey, still underway, undertakes a large-scale study of 25 early-type galaxies within a distance of 30 Mpc.

With the aid of wide-field imaging data, we can study the global properties of individual GC systems and hence the association with their host galaxies. These global properties include radial surface density, colour and azimuthal distributions, total number of GCs and specific frequency. The full radial extent of large GC systems can only be completely investigated with wide-field imaging data. From the radial surface density distributions of blue and red GCs, the characteristics of the subpopulations such as their extent and concentration (centrally or extended) can be investigated. A similar slope between host galaxy starlight and red GC surface density suggests a coeval formation (Bassino, Richtler & Dirsch 2006a; Faifer et al. 2011; Strader et al. 2011; Forbes, Ponman & O'Sullivan 2012a). The dark matter halo component of a galaxy is associated with the blue GC subpopulation (Forbes, Ponman & O'Sullivan 2012a; Forte, Vega & Faifer 2012), which shows their connection with the hidden dark matter (proposed by Côté et al. 1998). Forbes et al. (2012a) found good agreement between galaxy diffuse X-ray emission and the surface density of the blue GCs for nine ellipticals.

The two-dimensional spatial distribution of GC systems can be constructed with imaging data. Estimation of position angle (PA), ellipticities and two-dimensional substructures can be carried out. Most previous studies carried out using smaller telescopes (e.g. Rhode, Windschitl & Young 2010; Young, Dowell & Rhode 2012) are unable to probe very far down the GC luminosity function and thus yield too few GCs to properly separate the system in red and blue subpopulations. Literature studies of galaxies like NGC 4636 (Dirsch, Schuberth & Richtler 2005) and NGC 1316 (Gómez et al. 2001) show that the azimuthal distribution of red GCs closely matches that of the spheroid/bulge of the host galaxy. Such observations support the idea that the bulk of galaxy stars have a coeval origin with the red GC subpopulation (Wang et al. 2013). The total number of GCs can only be determined accurately from a complete radial surface density distribution. An advantage of wide-field imaging taken in good seeing conditions is a more accurate determination of specific frequency with reduced errors [e.g. for NGC 4365 S_N varies from 3.86 ± 0.71 (Peng et al. 2008) from small field of view of *Hubble Space Telescope* (*HST*) imaging to 7.75 ± 0.13 (Blom et al. 2012) with wide-field Subaru data].

With the global properties of a sample of GC systems, we are also equipped to study their global relations with the host galaxies. A relevant question to study is the (in)dependence of the GC formation efficiency on different environments. Recently, Tonini (2013) constructed a theoretical model to investigate GC bimodality. She predicted that the GC bimodality is a direct outcome of the hierarchical galaxy assembly. Also she predicted that a larger fraction of blue GCs can be found in early-type galaxies residing in higher density environments. However, using ACS Virgo Cluster Survey (ACSVCS) data Cho et al. (2012) studied the variation in the fraction of red GCs in field and cluster environments. They found that the fraction of red GCs was enhanced from field to high-density environment. Spitler et al. (2008) also studied the dependence of mass normalized blue GC number on environment for a sample of early-type galaxies. They concluded that the GC formation efficiency depends primarily on the galaxy mass and is nearly independent of the galaxy environment. In this paper, we also try to analyse these different results regarding the dependence of the GC formation efficiency on environment.

In short, this paper presents the results from a wide-field imaging study of the GC systems in three early-type galaxies, their global properties and their connection with the host galaxy properties. Also we have explored the correlations of the global properties of GC systems (including GC systems of other well-studied early-type galaxies) with host galaxy mass, galaxy effective radius and local environment density.

This paper is organized as follows. Our three sample galaxies are briefly presented in the following subsection. Section 2 presents observations, data reductions, photometry and the selection of GCs. Section 3 explores the different GC system properties such as radial density, colour distributions, azimuthal distribution, total number of GCs and specific frequency. Analysis of GC subpopulations and their connection with host galaxy properties are also described in Section 3. Section 4 discusses the relationship of GC system extent with galaxy stellar mass, effective radii and environment for a sample of ∼40 galaxies. Section 5 concludes with the main results and their implications for GC formation scenarios.

1.1 Sample galaxies

Our three galaxies of intermediate luminosity are taken from the ongoing SLUGGS survey (Brodie et al., in preparation) of 25 galaxies within 30 Mpc and are among the most elongated galaxies in the survey. The three galaxies reported here are among the most flattened in the SLUGGS survey and hence useful to search for trends between the flattening (ellipticity) of the GC system and the host galaxy. Table 1 records the basic data for the sample galaxies and an individual description for each galaxy follows.

1.1.1 NGC 720

NGC 720 is an X-ray bright, relatively isolated elliptical galaxy. The morphological classification is an E5 (de Vaucouleurs et al. 1991).

---

[1] http://sluggs.swin.edu.au/

Table 1. Basic data for the target galaxies. Right ascension and declination (J2000) are from NASA/IPAC Extragalactic Database (NED). The galaxy types are discussed in Section 1.1. The distance for NGC 720 is obtained from NED; NGC 1023 and NGC 2768 are from Cappellari et al. (2011). Total *V*-band magnitudes are obtained from de Vaucouleurs et al. (1991). The extinction correction for the *V* band is calculated from Schlegel, Finkbeiner & Davis (1998). The absolute total magnitude is derived from the *V*-band magnitude, distance and the extinction correction. Position angle and ellipticity of the galaxy major axis are given in the last columns and are obtained from HyperLeda (Paturel et al. 2003).

Name	RA (h:m:s)	Dec. (°:′:″)	Type	D (Mpc)	V_T (mag)	A_v (mag)	M_v^T (mag)	PA (°)	ϵ
NGC 720	01:53:00.5	−13:44:19	E5	23.4	10.18	0.05	−21.68	142	0.47
NGC 1023	02:40:24.0	+39:03:48	S0	11.1	9.35	0.20	−21.08	87	0.58
NGC 2768	09:11:37.5	+60:02:14	E/S0	21.8	9.87	0.14	−21.91	93	0.60

NGC 720 has been well studied in X-rays by Buote & Canizares (1994, 1996, 1997) and Buote et al. (2002). The X-ray studies showed an isophotal twist which is absent at optical wavelengths. NGC 720 is found to be a strong X-ray source with filaments extending from the nucleus of the galaxy and curving towards the south (Buote & Canizares 1996). Kissler-Patig, Richtler & Hilker (1996) studied the GC system of NGC 720 out to a galactocentric distance of 4.37 arcmin (30 kpc). They did not study the properties of GC subpopulations, only the total system. They found the GC system to resemble the host galaxy light distribution in terms of ellipticity, PA and surface density. In contrast, the properties of the GC system did not match those of the X-rays. Forbes et al. (2012a) found a similar slope for the X-ray surface brightness profile and the surface density of the blue GC subpopulation of NGC 720.

1.1.2 NGC 1023

NGC 1023 is a nearby S0 galaxy at a distance of 11.1 Mpc (Cappellari et al. 2011) An interesting aspect of this lenticular galaxy is its bluer eastern companion, NGC 1023A. H I maps of NGC 1023 show a high concentration of neutral hydrogen gas around NGC 1023A (Sancisi et al. 1984). Capaccioli, Lorenz & Afanasjev (1986) did not detect any traces of emission lines in the spectrum of NGC 1023, indicating no current star formation. Larsen & Brodie (2000) studied the central GCs of NGC 1023 using *HST* Wide Field Planetary Camera 2 (WFPC2) imaging. They found 221 GCs and a bimodal colour distribution. They also found the presence of red extended (effective radii > 7 pc) GCs, naming them ‘faint fuzzies’. Cortesi et al. (2011) have used the planetary nebulae (PNe) to analyse the kinematics of NGC 1023. They found that the kinematics of the galaxy resembles a spiral galaxy, supporting the theory of transformation of S0 galaxies from spiral galaxies. Young et al. (2012) studied the GC system of NGC 1023 using imaging data from the 3.5 m WIYN telescope and estimated the total number of GCs to be 490 ± 30, with $S_N = 1.7 \pm 0.3$. They also found a statistically significant bimodal colour distribution for the GC system.

1.1.3 NGC 2768

NGC 2768 is catalogued as a lenticular galaxy in the Carnegie Atlas of Galaxies (Sandage & Bedke 1994) and an elliptical E6 in the Third Reference Catalogue of Bright Galaxies (RC3; de Vaucouleurs et al. 1991). Crocker et al. (2008) traced the interstellar medium of NGC 2768 from CO emission, finding a molecular polar disc, which suggests a merger history for NGC 2768. Kundu & Whitmore (2001) studied the GC system of NGC 2768 using single *HST*/WFPC2 pointing and found a statistically significant bimodal colour distribution. Pota et al. (2013) performed a kinematic study of the GC systems of 12 early-type galaxies including NGC 2768. They found GC bimodality in $(R_c - z)$ colour. They also found that the rotation velocity of red GCs matches the galaxy stars, supporting coeval formation. Usher et al. (2012) have carried out a study of CaT metallicity distribution of NGC 2768 GCs, but did not find bimodality in the CaT metallicity for the GCs. The available photometry for the galaxy was poor and they obtained spectra only for a few GCs, which they propose as the reason for not detecting bimodality in metallicity. Forbes et al. (2012b) analysed the kinematics, combining PNe, GCs and galaxy starlight. They found similarity in the radial density distribution between red GCs, galaxy bulge PNe and galaxy starlight, strengthening the idea of coeval evolution. Kinematic studies of these three components up to 4 $R_{\rm e}$ showed good agreement between them.

2 DATA

2.1 Observations and reduction techniques

The imaging data for NGC 720 and NGC 2768 were taken using the Suprime-Cam (Miyazaki et al. 2002) imager mounted on the 8 m Subaru telescope. The instrument includes ten 2048 × 4096 CCD detectors with a pixel scale of 0.202 arcsec and a field of view of 34 × 27 arcmin^2. Multiple exposures were taken in a dithered pattern to avoid the blank regions due to gaps between CCDs. The observation log is tabulated in Table 2.

The Suprime-Cam Deep Field Reduction package 2, SDFRED2 (Ouchi et al. 2004) is utilized to carry out the pre-processing of the Suprime-Cam data. The pipeline includes scripts for flat-fielding, distortion and atmospheric dispersion corrections. The

Table 2. Log of observations.

Galaxy NGC	Filter	Obs. date *HST*[1]	Seeing (arcsec)	Telescope	Exp. time (s)
720	g	2008 Nov. 28	0.88	Subaru	1770
	i	2008 Nov. 28	0.98		1370
1023	g	2004 Sept. 10	0.71	CFHT	1232
	i	2004 Sept. 11	0.73		1100
2768	g	2011 Jan. 03	0.95	Subaru	4320
	r	2011 Jan. 04	0.77		1860
	i	2011 Jan. 04	0.75		1296

[1] Hawaii-Aleutian Standard Time.

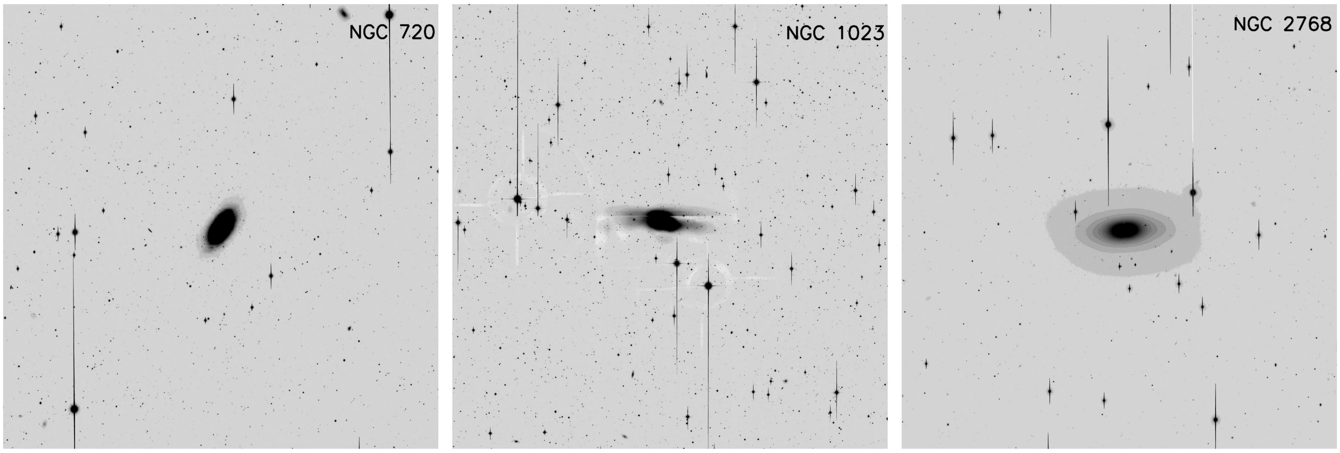

Figure 1. Wide-field images of three galaxies in the *i*-band filter taken from the ground-based telescopes. Each image covers on sky an area of 10 arcmin^2. NGC 720 and NGC 2768 were observed using the Subaru telescope while NGC 1023 was taken from the CFHT archive. North is up and east on the left.

pre-processed images were aligned and combined to form the mosaic image using a combination of software SExtractor (Bertin & Arnouts 1996), scamp (Bertin 2006) and swarp (Bertin et al. 2002).[2] The SExtractor run on the individual CCD images selects point sources with a 3σ threshold above the background level. The relative positions between the selected objects were matched with an astrometric reference catalogue [USNO or Sloan Digital Sky Survey (SDSS)] using the scamp software to generate the astrometric solution. Using the swarp software and the astrometric solution, the multiple CCD images were aligned and stacked to produce the mosaic image.

We have obtained a second photometric data set for NGC 2768 from the Hubble Legacy Archive. The data (HST ID: 9353) consist of one pointing taken in *F*435*W*(*B*), *F*555*W*(*V*) and *F*814*W*(*I*) filters using the Advanced Camera for Surveys (ACS) instrument installed on *HST*. The Wide Field Channel mounted on ACS consists of two 2048 × 4096 CCDs with 0.049 arcsec pixel scale and 3.37 × 3.37 arcmin^2 field of view. Jordi, Grebel & Ammon (2006) have given the transformation equations to convert the *B, V, I* magnitudes to the SDSS photometric system. The *B, V, I* magnitudes for all of the NGC 2768 objects are converted to *g, r, i* magnitudes.

We also acquired the central GC radial surface density distributions for NGC 720 from Escudero et al. (in preparation). This data set was observed in *g, r, i* filters using the Gemini Multi-Object Spectrographs (GMOS; Hook et al. 2004). NGC 720 was observed along with five other galaxies published in Faifer et al. (2011). A detailed description about the observations and data reduction is given in the same publication.

The wide-field imaging data for NGC 1023 were acquired from the Canada–France–Hawaii Telescope (CFHT) archive. Observations were taken with the MegaCam (Boulade et al. 2003) imager. The detector consists of a 9 × 4 mosaic of 2048 × 4612 CCDs with a scale of 0.187 arcsec giving a field of view of 0.96 × 0.94 square degree. A series of images taken in the *g* and *i* filters were processed through the MegaCam image stacking pipeline named MegaPipe (Gwyn 2008). MegaPipe includes the pre-processing (bias and dark subtraction, flat-fielding) of the images. The pipeline carries out an astrometric and photometric calibration for the MegaCam images. The individual CCD images were then mosaicked with the swarp software. Fig. 1 shows the wide-field images of NGC 720, NGC 1023 and NGC 2768 observed in the *i*-band filter using the ground-based telescopes.

2.2 Photometry

We modelled the galaxy light for the three galaxies and subtracted it from the corresponding mosaic image with the iraf task `ELLIPSE` keeping the centre, PA and ellipticity as free parameters. Here we remind the reader that the galaxy light-subtracted images are only used to improve source detection and not for any photometric analysis. The `ELLIPSE` parameters (PA and ellipticity) derived from the task match well with the values mentioned in HyperLeda (given in Table 1). Sources on images were identified and aperture photometry was carried out using the source finding software, SExtractor. SExtractor identifies a probable source only if it has a minimum of five adjacent pixels with a threshold level of 3σ above the local background. SExtractor estimates the total instrumental magnitude for the detected sources using the Kron (1980) radius in automatic aperture magnitude mode. For this, magnitudes within aperture sizes of 1–7 pixels, equivalent to 0.2–1.4 arcsec, are estimated for all the detected sources in the respective mosaic images. Depending on the seeing values for the respective filters, the extraction radius is determined and hence we obtain instrumental magnitudes. These instrumental magnitudes are corrected for the light outside the extraction radius, and finally SExtractor provides a list of point sources with positions and aperture-corrected magnitudes. We selected ∼20 bright stars within the colour range of $0.7 < (g - i) < 1.3$ in the individual galaxy images and obtained their magnitudes from the SDSS catalogues, in order to estimate the zero-points in each filter. These zero-points were applied to calibrate the magnitudes for all the point sources detected. Our final object lists have *g* and *i* magnitudes for all three galaxies, with additional *r* magnitudes for NGC 2768. The object magnitudes are corrected for Galactic extinction using Schlegel et al. (1998) (see Table 1). All magnitudes discussed hereafter are extinction corrected.

2.3 *HST*/WFPC2 GC catalogue for NGC 1023

Larsen & Brodie (2000) have published a list of 221 GCs in NGC 1023 observed with *HST* in the *V* and *I* filters. Their selection was primarily based on sizes, colour [i.e. $0.75 < (V - I) < 1.40$] and magnitudes (i.e. $20 < V < 25$). For uniformity between the

---

[2] http://www.astromatic.net/software/

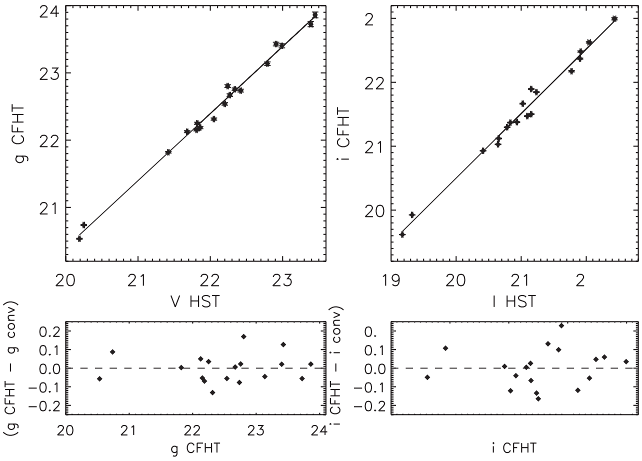

Figure 2. Transformation of NGC 1023 GC magnitudes from *HST* to CFHT photometric system. The top panels show the linear fits between *HST* magnitudes and CFHT magnitudes for the common GCs in *g* (left-hand panel) and *i* (right-hand panel) filters. The bottom panels show the difference between the measured (from CFHT) and converted magnitudes versus the measured magnitudes in the *g* (left-hand panel) and *i* (right-hand panel) filters.

catalogues, we converted the V and I magnitudes into the CFHT g and i magnitudes. Jordi et al. (2006) transformation equations require three band magnitudes whereas the *HST*/WFPC2 data contain only V and I magnitudes. In order to convert the magnitudes, we selected a set of bright objects [in the colour range $0.85 < (V - I) < 1.35$] in common between the two data sets, and the magnitudes are fitted with a linear bisector relation of the form

$$g_{\rm conv} = [(0.996 \pm 0.021) \times V_{\rm HST}] + (0.473 \pm 0.175) \quad (1)$$

$$i_{\rm conv} = [(1.009 \pm 0.031) \times I_{\rm HST}] + (0.304 \pm 0.113), \quad (2)$$

where $g_{\rm conv}$ and $i_{\rm conv}$ are CFHT filter equivalent magnitudes for the *HST V* and *I* magnitudes. The top panels in Fig. 2 show the magnitude conversion between the *HST* and the CFHT photometric systems. The bottom panels in Fig. 2 display the deviation between the measured ($g_{\rm CFHT}$ and $i_{\rm CFHT}$) and converted ($g_{\rm conv}$ and $i_{\rm conv}$) magnitudes. The root-mean-square deviations of converted magnitudes (using equations 1 and 2) from the corresponding measured CFHT magnitudes are 0.07 and 0.12 mag with no obvious systematic trend. This conversion is used to transform the *HST* photometric system to the CFHT system for the GCs of Larsen & Brodie (2000). We also checked the colour transformation between the two photometric systems and found no systematic trend.

2.4 GC selection

2.4.1 NGC 720

The GC selection for NGC 720 is carried out on object size, magnitude and colour of individual objects. Initially however, the source position matching between the Subaru g- and i-band images removes spurious detections (e.g. cosmic rays) on the individual images. To determine the object size, we measure the flux in two apertures. Objects with surplus amount of light beyond the extraction aperture radius are removed from the GC list. As GCs appear as point sources at the distance of NGC 720, the probable GCs have a minimum magnitude difference between the extraction aperture and the adjacent aperture. A further selection of objects is carried out in the i band, i.e. $20.6 \leq i \leq 24$ [at the distance of 23.4 Mpc, objects brighter than $i = 20.6$ include ultra-compact dwarfs (Brodie et al. 2011), while objects fainter than $i = 24$ have magnitude errors greater than 0.15]. Final selection of NGC 720 GCs is based on the $(g - i)$ colour of individual objects, i.e. $0.6 \leq (g - i) \leq 1.3$. In the SLUGGS survey, we have a list of spectroscopically (velocity) confirmed GCs for each of the survey galaxies. Hence, we are able to check the reliability of GC selection for all the three sample galaxies.

2.4.2 NGC 1023

The data for NGC 1023 include CFHT g- and i-band photometry and a catalogue of 221 GCs from *HST* (Larsen & Brodie 2000). The GC system of NGC 1023 is identified based on the same selection criteria followed for NGC 720 Suprime-Cam data. Matching of object positions between the observed g- and i-band images cleared false detections from the list. The i-band magnitude selection for NGC 1023 GCs is $18.9 \leq i \leq 23.0$ based both on the distance to NGC 1023 and on the error in the measured i-band magnitude. A final selection is made in colour by selecting sources in the same colour range as used by Larsen & Brodie (2000), i.e. $0.65 \leq (g - i) \leq 1.3$.

2.4.3 NGC 2768

The data for NGC 2768 include g-, r- and i-band Subaru imaging. False detections are primarily eliminated from the object list by matching the source position with 0.1 arcsec accuracy between the three bands. Point source objects are chosen based on the magnitude difference between the extraction and the adjacent aperture. As the data set for NGC 2768 consists of three-band data, an additional selection based on two-colour space is introduced [i.e. $(g - i)$ versus $(r - i)$]. We adopted a similar GC selection process in the colour–colour diagram as used by Spitler et al. (2008) and Blom et al. (2012). It is evident from earlier studies, namely fig. 6 in Blom et al. (2012) and fig. 3 in Pota et al. (2013), that the GCs populate a particular region in the colour–colour diagram. These GCs along with neighbouring objects showing a 2σ deviation from the selected region are chosen as final GC candidates. The i-band magnitude cut for NGC 2768 is $20.4 \leq i \leq 24.0$. A second set of data for NGC 2768 comes from *HST*/ACS covering the central 2.1 arcmin region. The GCs from the *HST*/ACS imaging are selected in the same colour–colour diagram mentioned above for the Subaru imaging.

3 ANALYSIS OF GC SYSTEMS

3.1 Surface density profiles

The one-dimensional radial distribution of a GC system is revealed by its surface density profile. The surface density for each radial bin is estimated by fixing a similar number of GCs per circular bin and dividing by the effective covered area. The area coverage in each annulus is corrected for two factors: the presence of saturated stars and the annular area outside the image. The errors associated with the surface density distribution are given by Poisson statistics.

A combination of a Sérsic profile and a background parameter is fitted to the GC surface density distribution. The fitted profile can be written as

$$N(R) = N_e \exp\left[-b_n \left(\frac{R}{R_{\rm e}}\right)^{\frac{1}{n}} - 1\right] + {\rm bg}, \quad (3)$$

where N_e is the density of the GCs at the effective radius R_e, n is the Sérsic index or the shape parameter for the profile, b_n is given by the term $1.9992n - 0.3271$ and bg represents the background parameter. The background values obtained for the three GC systems are then subtracted from the respective radial density distribution which is shown in all density distribution plots.

3.1.1 NGC 720

Fig. 3 displays the surface density profile for NGC 720 using the Suprime-Cam and GMOS data, fitted with a Sérsic profile. The radial coverage of GMOS data reaches out to 5.6 arcmin and overlaps with the Suprime-Cam data which is detected out to a radius of ∼18 arcmin. The GCs brighter than the turnover magnitude ($i = 23.7$) are selected to retrieve the radial surface density distribution. A constant value of 0.98 objects per arcmin^2 is reached at a galactocentric radius of 9.8 ± 0.8 arcmin suggesting that the background is obtained. At a distance of 23.4 Mpc, the GCs extend to at least 68 ± 6 kpc from the centre of the galaxy. The parameter values for the fitted profile are reported in Table 3. As seen from Fig. 3, the data sets from the Gemini and Subaru telescopes are generally consistent with each other without applying any manual adjustment. Kissler-Patig et al. (1996) have studied the radial density distribution of NGC 720 GCs using the 2.2 m telescope at the European Southern Observatory. They estimated that the GC system reaches the background at a galactocentric distance of 2.67 arcmin. This appears to be an underestimation of the true extent by a factor of ∼3.

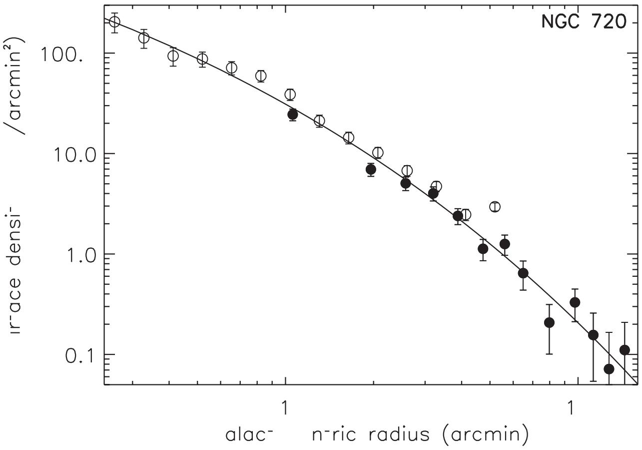

Figure 3. Surface density profile for the GC system of NGC 720. The plot displays the Gemini (open circles) and Subaru (filled circles) data. The GCs selected within the turnover magnitude limit, $i = 23.7$, are employed to derive the radial surface density values. The surface density reaches the background level around 9.8 ± 0.8 arcmin (∼15 R_e) with 0.98 objects per arcmin^2. The solid line shows the fitted Sérsic profile for the GC surface density.

Table 3. Fitted parameters for the surface density of NGC 720, NGC 1023 and NGC 2768 GC systems. The last column in the table presents the extent of the GC system in each galaxy.

Name NGC	R_e (arcmin)	n	bg (arcmin^{-2})	GCS ext. (arcmin)
720	1.97 ± 0.34	4.16 ± 1.21	0.98 ± 0.06	9.8 ± 0.8
1023	1.00 ± 0.35	3.15 ± 2.85	1.27 ± 0.12	6.2 ± 0.5
2768	1.66 ± 0.23	3.09 ± 0.68	0.61 ± 0.04	9.9 ± 0.5

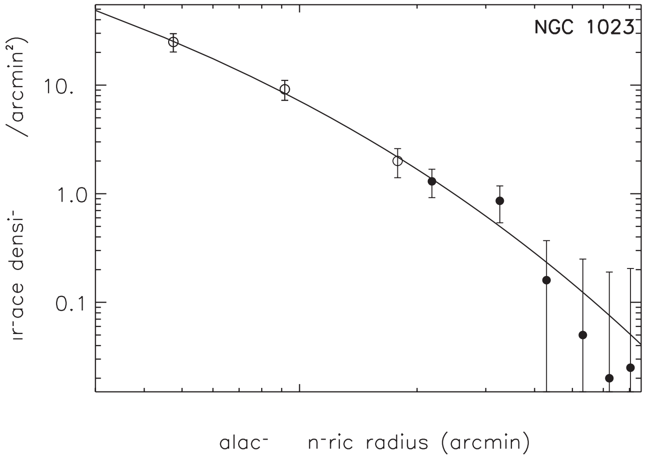

Figure 4. Surface density profile for the GC system of NGC 1023. The plot shows *HST* (open circles) and CFHT (filled circles) data. The limiting magnitude for the two data sets is the turnover magnitude, i.e. $i = 22.0$. The surface density of the GC system reaches the background level around 6.2 ± 0.5 arcmin (∼8 R_e) with 1.27 objects per arcmin^2. A Sérsic profile is fitted and is shown with a solid line.

This likely demonstrates our high-quality wide-field imaging and its ability to remove contamination.

3.1.2 NGC 1023

We created a radial surface density plot for NGC 1023 using the GCs from the *HST* at the very centre and the CFHT for the outer regions. Larsen & Brodie (2000) identified a third set of GCs called red extended GCs or faint fuzzies. For the calculation of surface density, the faint fuzzies are excluded (i.e. objects with $V > 22.8$) as the turnover magnitude limit is $i = 22.0$. The area corrections are applied to account for the detector shape of *HST* and for saturated stars in the CFHT image. Fig. 4 shows a plot of surface density for the NGC 1023 GCs using *HST* and CFHT data. The GC surface density for NGC 1023 is fitted with equation (3) and fitted parameters are given in Table 3. The *HST* observations are limited to 2.2 arcmin radius and the CFHT observations extend to 15 arcmin from the centre of the galaxy. At a galactocentric radius of 6.2 ± 0.5 arcmin, the GC surface density flattens to a constant value of ∼1.27 objects per arcmin^2. From the centre of NGC 1023, the GCs reach an extent of 20 ± 2 kpc. The *HST* and CFHT data have not been adjusted in surface density and are consistent with each other in the region of overlap (when the two data are cut at the turnover magnitude). This overlap between *HST*- and ground-based telescopes is a representation of data quality. Young et al. (2012) investigated the GC system of NGC 1023 using the 3.5 m WIYN telescope. The radial extent of the GC system was estimated by them to be 6.3 ± 0.8 arcmin. Thus, Young et al. (2012) and our work are in agreement on the radial extent of the NGC 1023 GC system.

3.1.3 NGC 2768

Fig. 5 displays the radial distribution of the GC system of NGC 2768. The data points in the inner 2.1 arcmin radius of the galaxy were obtained from the *HST* data and the area beyond that was covered by the Subaru data. The data points shown in Fig. 5 are generated from the GCs with $i < 23.3$ (i.e. the turnover magnitude).

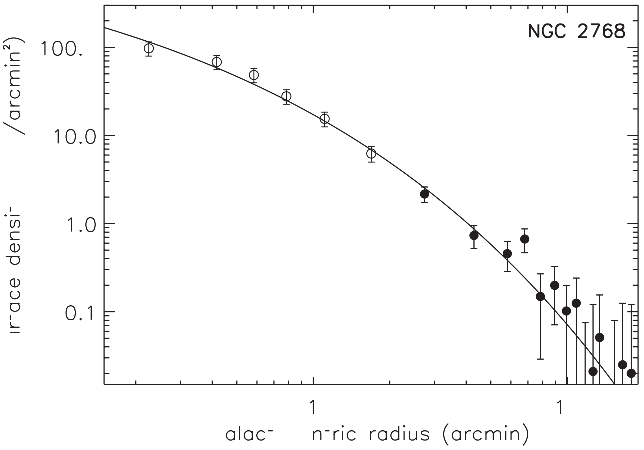

Figure 5. Surface density profile for the GC system of NGC 2768. The plot shows *HST* (open circles) and Subaru (filled circles) data. The GCs within the turnover magnitude limit, $i = 23.3$, are selected for the density distribution. NGC 2768 GCs reach the background at a galactocentric distance of 9.9 ± 0.5 arcmin ($\sim$10 R_e) with 0.61 objects per arcmin^2. The solid line represents the Sérsic profile fitted on the GC density distribution.

The *HST* data points are corrected for the detector shape. The presence of saturated stars in the inner annular radii and the area outside the detector was taken into account in the area calculation for the Subaru data points. The GC system of NGC 2768 reaches a background value of 0.61 objects per arcmin^2 at a galactocentric distance of 9.9 ± 0.5 arcmin. The surface density distribution of the GCs is fitted with a Sérsic profile and is shown in Fig. 5. The extent of the GC system of NGC 2768 is at least 63 ± 3 kpc. Since both data sets are cut at the turnover magnitude, the good overlap between *HST* and Subaru data sets confirms the magnitude completeness of the Subaru data. We are unable to find any previous work which has studied the GC extent for this galaxy.

3.2 Colour–magnitude diagrams

The top panels in Fig. 6 show the colour–magnitude diagrams (CMDs) of GC candidates for the sample galaxies, based on the selection discussed in Section 2.4. The CMDs display all the detected objects brighter than $M_i = -7.75$ mag (0.5 mag fainter than the turnover magnitude) for the respective galaxies. The bottom panels display the $(g - i)$ colour histograms of the same GC candidates along with the background contamination for the respective galaxies. In this figure, we have displayed only the data from the wide-field imaging and not from the space-based data. Also the histograms represent only the GC candidates detected above the turnover magnitude. In order to estimate the colour distribution of background objects within the GC extent, we have made use of the objects detected outside the GC system extent. First, the colour distribution of the objects outside the GC extent is analysed and corrected for the relevant areal coverage. Then this colour distribution (shown in lower panels of Fig. 6) is subtracted from the corresponding GC system colours to obtain the uncontaminated GC colour distribution. The colour distribution of the background objects generally shows a broad colour range and does not strongly affect the GC subpopulation peaks.

All CMDs have displayed objects detected above the magnitude $M_i = -7.75$ mag. The top-left panel shows the CMD for NGC 720 GC candidates detected within a galactocentric radius of 9.8 arcmin (see Section 3.1), observed using the Subaru/Suprime-Cam telescope. The colour histogram of detected GC candidates above the turnover magnitude along with the background is displayed in the bottom-left panel. The CMD for the NGC 1023 GC candidates is plotted in the top-middle panel, detected from the CFHT/MegaCam

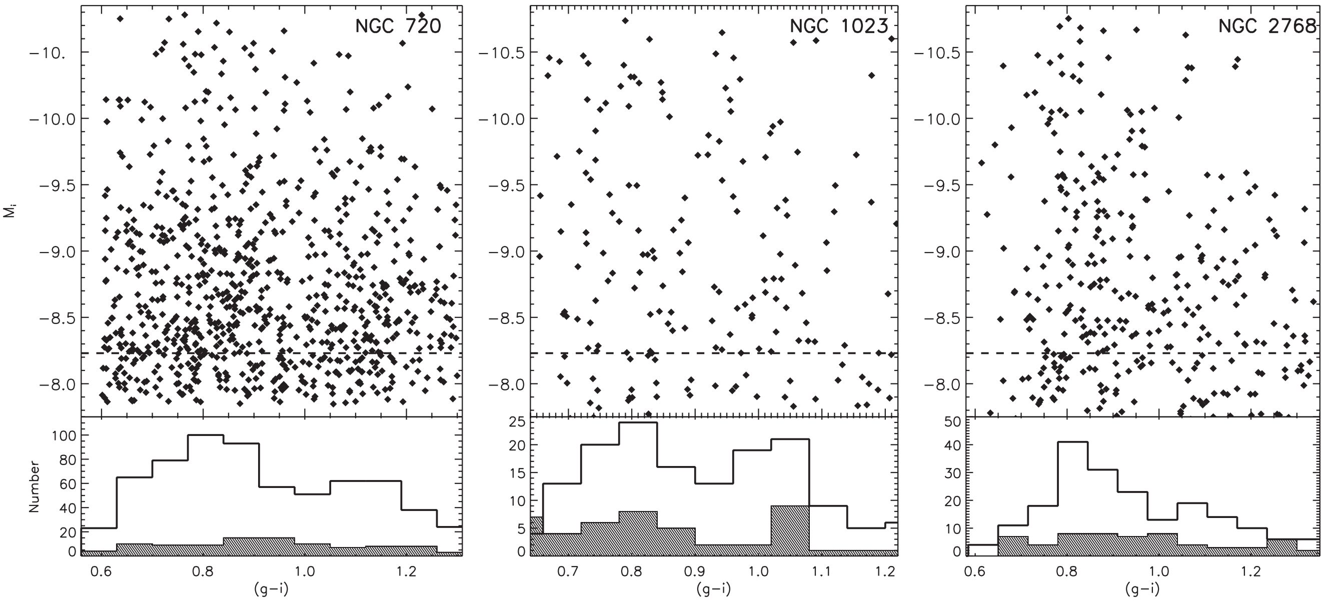

Figure 6. Colour–magnitude diagrams for the selected GC candidates using wide-field data. GC candidates shown in the figure include objects brighter than $M_i = -7.75$ mag within the measured GC system extent. The turnover magnitude in the i filter is $M_i = -8.23$ mag, shown as a dashed line in all three top panels. The top-left panel shows the GC candidates of NGC 720 observed using Subaru/Suprime-Cam. The open histogram is plotted in the bottom-left panel representing the Subaru data with objects detected above the turnover magnitude. The shaded area represents the estimated background for the Subaru data. The top-middle panel shows the GC candidates of NGC 1023 observed using CFHT/MegaCam. The bottom-middle panel displays the histogram of GC candidates from the CFHT (open) and the background contamination (shaded). The top-right panel shows the GC candidates of NGC 2768 using Subaru/Suprime-Cam. The histogram of the GC candidates (open) for NGC 2768 is shown along with the background (shaded) in the bottom-right panel.

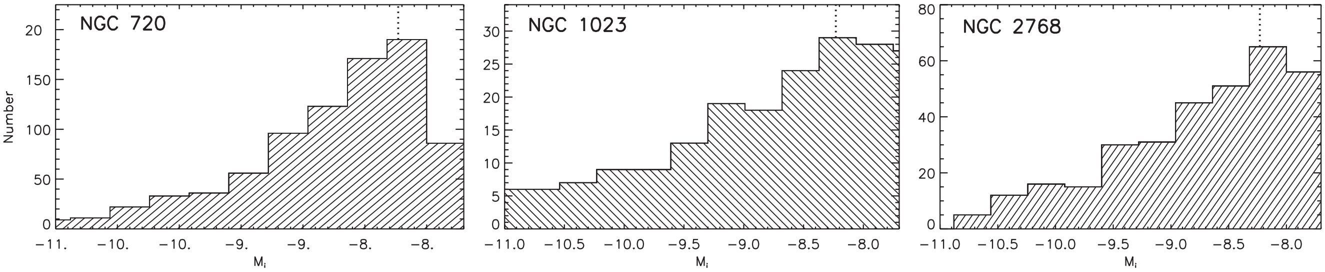

Figure 7. GC luminosity function in the *i*-band filter. The histograms represent the GC luminosity function of the GC systems detected for the individual galaxies. The histograms only include the GCs detected till the GC system extent estimated from the radial surface density distributions. The dotted line at $M_i = -8.23$ represents the turnover magnitude in the *i*-band filter.

data. As the surface density of GC candidates reaches the background at 6.2 arcmin from the centre, the CMD is plotted with the objects within that radius only. The bottom-middle panel displays the colour histogram for the GC candidates and the background. The top-right panel in Fig. 6 displays the CMD for the NGC 2768 GC candidates. The diagram exhibits the GCs detected using Subaru/Suprime-Cam data. Only the GC candidates detected within a galactocentric radius of 9.9 arcmin are included in the plot, and the respective colour histogram for GC candidates along with background is shown in the bottom-right panel. The GC luminosity function for the detected GCs is plotted in Fig. 7 for the three galaxies.

3.3 GC bimodality

3.3.1 *Colour histograms*

Fig. 8 illustrates the colour histograms of GCs corrected for the background contamination. The background contaminations for each GC system (shown in the bottom panels of Fig. 6), after area correction, are subtracted and the final GC colour distribution is shown. The final list of detected GCs above the turnover magnitude after background contamination correction includes 554 (Subaru) for NGC 720, 62 (*HST*) and 105 (CFHT) for NGC 1023, and 147 (*HST*) and 139 (Subaru) for NGC 2768.

The left-hand panel of Fig. 8 shows the NGC 720 GC colour histogram using Subaru/Suprime-Cam data. The galaxy shows a clear distinction between the blue and red subpopulations with more blue than red GCs. The blue and red GC subpopulations of NGC 720 peak in colour around $(g - i) = 0.8$ and 1.1, respectively. The middle panel shows the colour histogram for NGC 1023 GCs using *HST*/WFPC2 and CFHT/MegaCam data. The colour distribution shows a bimodal nature with two peaks around $(g - i) = 0.8$ and 1.05. The right-hand panel represents the colour histogram of NGC 2768 GCs detected using *HST*/ACS and Subaru/Suprime-Cam data. Both data sets show a bimodal colour distribution. The blue and red subpopulations peak in colour at $(g - i) = 0.8$ and 1.1, respectively.

The CMDs and colour histograms for the three sample galaxies strengthen the bimodal distribution of GCs for the galaxies. Kissler-Patig et al. (1996) studied the GC system of NGC 720, but did not detect bimodality. Larsen & Brodie (2000) confirm the bimodal distribution for NGC 1023 GCs using the *HST*/WFPC2 data. Later, Young et al. (2012) reconfirmed the presence of multiple subpopulations in NGC 1023 using WIYN data. NGC 2768 was the only galaxy detected with a clear bimodal colour distribution in a survey of 29 S0 galaxies by Kundu & Whitmore (2001).

3.3.2 *Gaussian mixture modelling*

Gaussian mixture modelling (GMM) is an algorithm to statistically quantify whether a distribution is unimodal or multimodal (Muratov & Gnedin 2010). The well-known Kaye's mixture model (KMM; Ashman, Bird & Zepf 1994) algorithm is among the general class of algorithms of GMM. Based on three statistics, the GMM signifies the presence of a multimodal distribution over unimodal. They are (1) confidence level from the parametric bootstrap method (low values indicate a multimodal distribution), (2) separation (D) of the means relative to their widths ($D > 2$ implies a multimodal distribution) and (3) kurtosis of the input distribution (negative kurtosis for multimodal distributions).

NGC 720. The GMM algorithm fit to the NGC 720 GC data gives a bimodal colour distribution with two peaks at

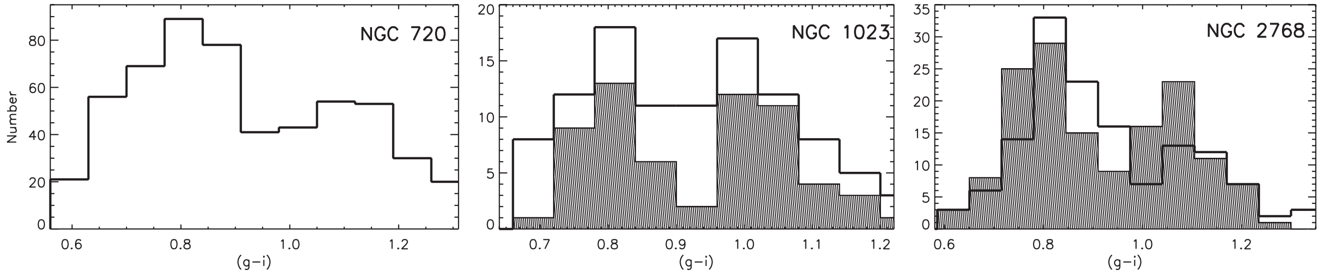

Figure 8. Colour histograms of GCs after the correction for background contamination. The estimated background contamination for the respective GC system is subtracted from the total GCs and the corrected GCs are represented in histograms. The left-hand panel shows the final GCs of NGC 720 detected using Subaru/Suprime-Cam. The histogram shows a clear bimodal colour distribution for NGC 720. The middle panel shows the GCs of NGC 1023 observed using *HST*/WFPC2 (shaded area) and CFHT/MegaCam (open area) data. The right-hand panel shows the GCs of NGC 2768 using *HST*/ACS (shaded area) and Subaru/Suprime-Cam (open area). The background subtraction has improved the colour histograms shown in Fig. 6 and now the peaks for the blue and red subpopulations are more distinctly seen.

$(g-i) = 0.793 \pm 0.010$ and 1.125 ± 0.012. The widths for the blue and red GCs are 0.104 and 0.090, respectively. The GMM algorithm partitions the total GC system into 64 per cent blue and 36 per cent red GC subpopulations. The parametric bootstrap method rules out the unimodal distribution with a confidence level better than 0.01 per cent (implying that a multimodal distribution is supported with >99.9 per cent probability) and $D = 3.42 \pm 0.16$ for the NGC 720 GCs.

NGC 1023. Using GMM on the *HST* data, the GC system of NGC 1023 has $D = 3.55 \pm 0.53$ supporting multimodality. The peaks of the blue and red subpopulations are $(g - i) = 0.785 \pm 0.015$ and 1.017 ± 0.022, respectively. The estimated widths for the subpopulations are 0.033 and 0.086. The total GC system consists of 38 per cent blue and 62 per cent red subpopulations. The heteroscedastic fit for the GCs of NGC 1023 from CFHT data gives a blue peak at $(g-i) = 0.799 \pm 0.020$ and a red peak at 1.038 ± 0.022. The GMM algorithm divides the total GCs into 43 and 57 per cent blue and red GCs, respectively. The blue and red peaks have widths of 0.069 and 0.091, respectively. GMM provides similar peak values for the subpopulations from the two data sets. Larsen & Brodie (2000) give the peak values of two subpopulations from the KMM test, i.e. $(V-I) = 1.02$ and 1.25, which are in reasonable agreement with the values derived from GMM, i.e. $(V-I) = 0.99 \pm 0.01$ and 1.26 ± 0.02.

NGC 2768. The GMM algorithm gives a multimodal colour distribution for the NGC 2768 GC system from the *HST* data. The blue and red subpopulations peak in colour around $(g - i) = 0.821 \pm 0.017$ and 1.101 ± 0.025, respectively. GMM provides the widths of the two subpopulations as 0.085 and 0.109. The value of D statistic is greater than 2.89, supporting two well-separated subpopulations for the NGC 2768 GC system. We then applied the GMM algorithm to the GC colours from the Subaru imaging. The heteroscedastic split in GCs peaks at $(g - i) = 0.819 \pm 0.015$ and 1.076 ± 0.017 with respective widths of 0.075 and 0.079 for the two subpopulations. The separation between two subpopulations is 3.65, and it supports bimodal distribution. The total GC system is divided into 65 per cent blue and 35 per cent red subpopulations.

3.3.3 *Colour–metallicity transformation*

Usher et al. (2012) give the colour–metallicity relation derived from an analysis of 903 GCs. The relation for GCs with $(g - i) > 0.77$ is of the form

$$[\mathrm{Z/H}] = [(3.49 \pm 0.12) \times (g-i)] + (-4.03 \pm 0.11). \qquad (4)$$

We have converted the peak colours for the GC subpopulations of the three galaxies into metallicity and listed them in Table 4. The peak metallicity for the blue and red subpopulations agrees with the GC colour/metallicity–galaxy luminosity relation (Peng et al. 2006; Faifer et al. 2011).

Table 4. The peak values of colour for the blue and red GC subpopulations derived from GMM. The colour–metallicity relation given by equation (4) is used to derive the corresponding metallicity shown below. For NGC 1023 and NGC 2768, the peak colour and metallicity values from both data are recorded.

Galaxy NGC	Blue GCs $(g-i)$	Blue GCs [Z/H]	Red GCs $(g-i)$	Red GCs [Z/H]
720	0.793 ± 0.010	-1.26 ± 0.07	1.125 ± 0.012	-0.10 ± 0.08
1023	0.785 ± 0.015	-1.29 ± 0.10	1.017 ± 0.022	-0.48 ± 0.15
	0.799 ± 0.020	-1.24 ± 0.14	1.038 ± 0.022	-0.41 ± 0.15
2768	0.821 ± 0.017	-1.16 ± 0.12	1.101 ± 0.025	-0.19 ± 0.17
	0.819 ± 0.015	-1.17 ± 0.10	1.076 ± 0.017	-0.27 ± 0.12

3.4 GC subpopulations

With our high-quality photometric data, we are able to separate the GC subpopulations and investigate their properties. Fig. 9 shows the two-dimensional images of the three galaxies after the subtraction of galaxy stellar light. The positions of the blue and red GCs are displayed on each galaxy image. Only the GCs detected within the turnover magnitude are used in the study of GC subpopulations. First, the surface density distribution of GC subpopulations with galactocentric radius is analysed. For this, the GC system of NGC 720 is classified into blue and red subpopulations dividing at the colour $(g-i) = 0.98$ (the colour at which the Gaussian distributions for the two subpopulations cross in the GMM fit). The subpopulations are separately binned in galactocentric radius and the surface density values are calculated. Fig. 10 displays the estimated values of background-subtracted surface density for the blue and red GCs along with the total system. The Gemini and Subaru data are merged together to obtain the distribution from a galactocentric radius of 0.18–18 arcmin. The surface densities are fitted with a Sérsic profile (see equation 3). The fitted parameters for the blue and red GCs are recorded in Table 5. The blue subpopulation has a density enhancement over the red subpopulations over the whole range of radius except in the central 0.9 arcmin. The effective radius for the blue subpopulation is larger than that for the red subpopulation.

Due to the small number of detected GCs within the turnover magnitude, we are unable to fit the distribution of GC subpopulations of NGC 1023.

For NGC 2768, the GCs are classified into blue and red subpopulations at $(g - i) = 0.96$ (from the GMM fit). The background-subtracted surface density values for the blue and red subpopulations are plotted in Fig. 11. Both the *HST* and Subaru data are incorporated in the figure. The radial density distributions for blue and red subpopulations are fitted with a Sérsic profile. Table 5 tabulates the fitted parameters for the blue and red GC density distributions. The blue and red GCs have similar density profiles, with the more extended blue subpopulation.

3.5 Radial colour distribution

The blue and red subpopulations of NGC 720 are separated at a colour of $(g - i) = 0.98$. The average colour in each radial bin is estimated separately for blue and red subpopulations. Neither the red nor the blue subpopulations from the Subaru data reveal a colour gradient. The average colour values for the two subpopulations with galactocentric radius are displayed in Fig. 12.

The separation between the two subpopulations for NGC 1023 GCs is $(g - i) = 0.88$ (from the GMM fit) for the *HST* and the CFHT data. The averaged colour values in each radial bin for the *HST* and the CFHT data sets are plotted in Fig. 13. The individual GCs from the *HST* and CFHT are also plotted in this figure. A positive colour gradient is visible for the *HST* red subpopulation (slope = 0.028 ± 0.009 mag arcmin^{-1}).

Fig. 14 shows the radial colour distribution for the blue and red GCs of NGC 2768 to a galactocentric distance of 12 arcmin from the centre. The GCs are categorized into blue and red subpopulations at $(g - i) = 0.96$. This figure also displays the individual GCs from the *HST* and the Subaru data. The radial colour distribution from the Subaru data does not show any statistically significant radial trend, which might be caused by the contamination from the

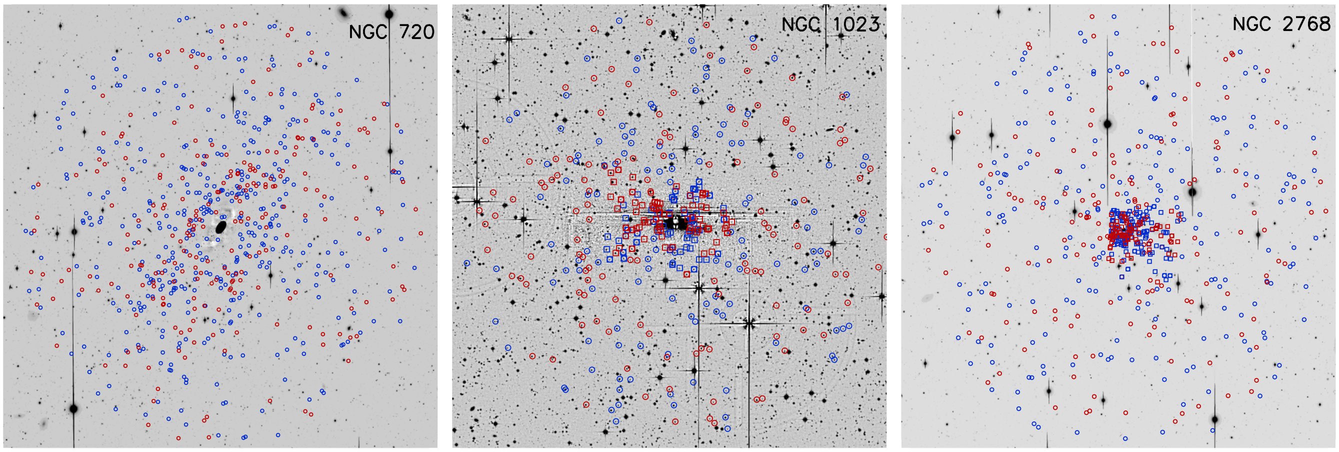

Figure 9. Two-dimensional sky images of three galaxies: NGC 720, NGC 1023 and NGC 2768. The galaxy stellar light is subtracted from the individual images with north up and east on the left. Each galaxy image covers an area of 10, 6.3 and 10 square arcmin centred on the galaxy, respectively, for NGC 720, NGC 1023 and NGC 2768. The blue and red open circles represent the positions of the blue and red GC candidates detected from the ground-based telescopes, whereas the blue and red open squares represent the positions of the blue and red GC candidates detected from the *HST*.

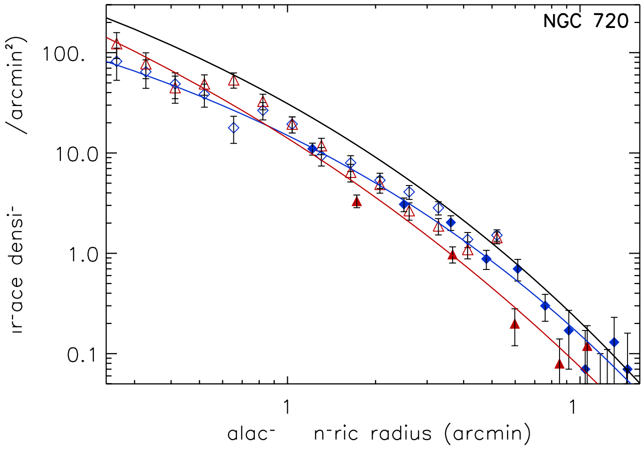

Figure 10. GC subpopulations of NGC 720. Surface densities for the blue (diamonds) and red (triangles) GCs of NGC 720 are shown. The open and the filled symbols represent the Gemini and the Subaru data, respectively. A Sérsic profile is fitted to the three GC distributions and is displayed in respective colour solid lines along with the total system in a black solid line.

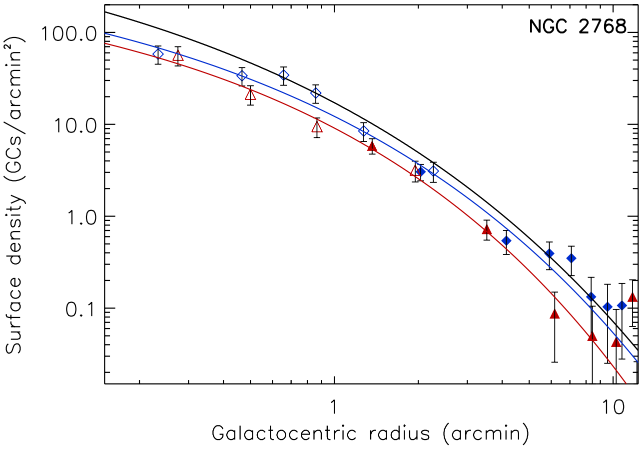

Figure 11. GC subpopulations of NGC 2768. The data sets include *HST* (open symbols) in the inner 2.1 arcmin radius and Subaru (filled symbols) to 20 arcmin. The radial density distribution for the blue (diamonds) and red (triangles) GCs is shown. The solid lines denote the Sérsic profiles for the two subpopulations and the total system in black solid line.

Table 5. Fitted parameters for the surface density of blue and red GC subpopulations of NGC 720 and NGC 2768. We are not able to fit the GC subpopulations of NGC 1023.

NGC	GCs	R_e (arcmin)	n	bg (arcmin^{-2})
720	Blue	3.93 ± 2.30	4.78 ± 2.30	0.63 ± 0.06
	Red	1.33 ± 0.31	5.55 ± 2.53	0.39 ± 0.04
2768	Blue	1.83 ± 0.27	2.78 ± 0.64	0.33 ± 0.03
	Red	1.50 ± 0.23	2.53 ± 0.79	0.25 ± 0.05

ground-based data. But the inner blue GCs from the *HST* data show a slight negative slope (0.007 ± 0.002 mag arcmin^{-1}).

The radial colour distribution is an important tool to study different GC formation scenarios. In the cases of NGC 1407 and M87, both GC subpopulations show a negative colour gradient, supporting an in situ dissipative formation scenario for the GCs. Beyond a transition radius, the GCs do not show a colour gradient. The GCs exterior to the transition region may be formed by ongoing accretion/mergers. The data used for the NGC 1407 study (Forbes et al. 2011) came from three-band imaging with subarcsecond seeing using the Subaru telescope. The colour gradient observed for the M87 GCs (Harris 2009b) was taken with multiband filters using the CFHT and the seeing for the observation was 0.8 arcsec.

3.6 Azimuthal distribution

We study the azimuthal distribution of the GC systems and their blue and red subpopulations. The PAs of individual GCs (θ) are estimated from the right ascension and declination from the centre of the galaxy keeping 0° for north and measuring counter-clockwise. We binned the GCs in wedges of 18° and fitted a profile (McLaughlin, Harris & Hanes 1994) of the form

$$\sigma(R,\theta) = kR^{-\alpha}\left[\cos^2(\theta - \mathrm{PA}) + (1 - {}^2)^{-2}\sin^2(\theta - \mathrm{PA})\right]^{-\alpha/2} + \mathrm{bg}, \tag{5}$$

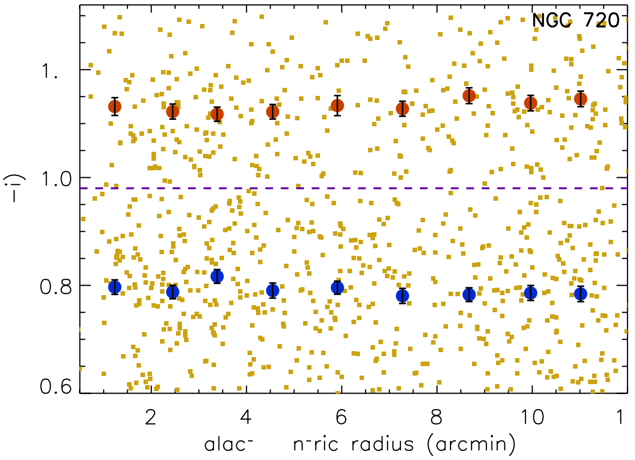

Figure 12. Colour distribution of the NGC 720 GC system with galactocentric radius. The individual GCs from the Subaru data are represented by yellow squares. The mean colours over particular bins in radius are shown as filled circles for Subaru data. The separation for blue and red GCs is shown with a dashed line at $(g - i) = 0.98$.

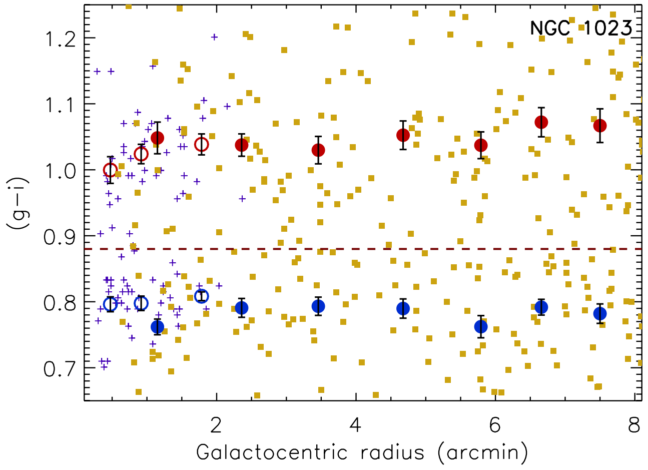

Figure 13. Colour distribution of the NGC 1023 GC system with galactocentric radius. The plot shows the average colour for the blue and red subpopulations using *HST* (open circles) and CFHT (filled circles) data. The individual GCs are represented by plus signs (*HST*) and squares (CFHT). The separation between the blue and the red GCs is shown with a dashed line at $(g - i) = 0.88$. The blue GCs show a constant colour with galactocentric radius, while the red GCs show a positive slope (0.028 ± 0.009 mag arcmin^{-1}) in the inner region and a constant colour for larger radii.

where $\sigma(R, \theta)$ is the azimuthal distribution of GCs at radius R and angle θ, α is the power-law index fitted to the surface density of GCs, bg is the background estimated from the Sérsic fits (see Section 3.1) and k is the normalization constant. The profile is iterated with the position angle of the GC system (PA) and the ellipticity ( ) as free parameters.

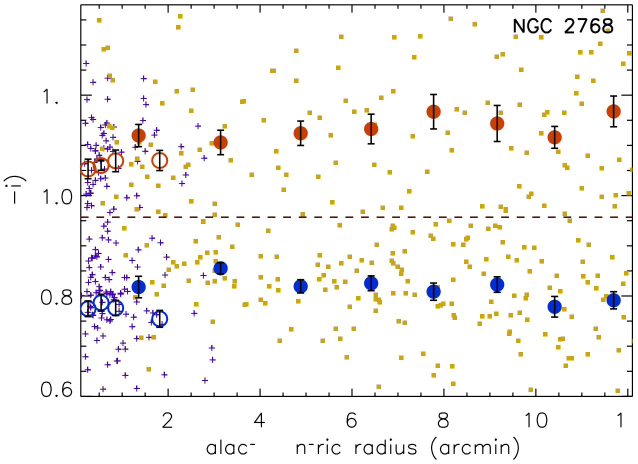

Figure 14. Colour distribution of the NGC 2768 GC system with galactocentric radius. The *HST* (open circles) and the Subaru (filled circles) data are incorporated in this figure. The average colour values in radial bins for the blue and the red subpopulations are represented by blue and red circles, respectively. The individual GCs from the *HST* (plus signs) and the Subaru (squares) are also displayed in the figure. The separation for blue and red GCs is shown with a dashed line at $(g - i) = 0.96$. The blue GCs selected from the *HST* data show a slight negative gradient with a slope of 0.007 ± 0.002 mag arcmin^{-1}.

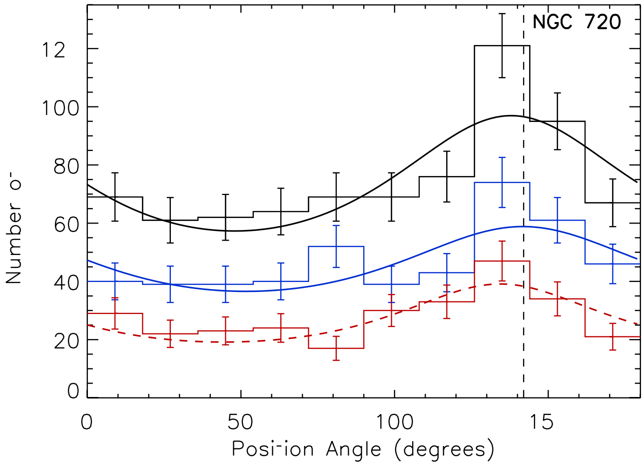

Figure 15. Azimuthal distribution of NGC 720 GCs. The histograms in black, blue and red represent the azimuthal distribution of total, blue and red GCs of NGC 720, respectively. The distribution is fitted with the profile given by equation (5) which is also plotted in the figure as solid (total system), dotted (blue subpopulation) and dashed (red subpopulation) lines. The host galaxy starlight (dashed vertical line) is aligned at a PA of 142° ± 5° which matches with the total system, the blue and red subpopulations of GCs.

3.6.1 *NGC 720*

For NGC 720, the PA of the galaxy light is 142° and the number of GCs in the azimuthal distribution peaks around 138° for the total GC population (see Fig. 15). The ellipticity value determined for the total GC system is 0.28 ± 0.06, while the galaxy light has an ellipticity of 0.47 ± 0.05. The GC system of NGC 720 matches with the galaxy light in PA but not in ellipticity. The azimuthal distribution is also determined for the blue and red subpopulations and recorded in Table 6. Both the blue and red subpopulations are aligned along the PA of the galaxy light. Also the ellipticity of the red subpopulation is in good agreement with the galaxy stellar light. Kissler-Patig et al. (1996) studied the shape of the GC system and the host galaxy. They estimated the PA and ellipticity for the GC system as 147° ± 10° and 0.5 ± 0.1, whereas the starlight had 142° ± 3° and 0.45 ± 0.05, respectively. We conclude that our findings about the PA and ellipticity of the GC system of NGC 720 match well with Kissler-Patig et al. (1996). They have also found that the PA (115° ± 15°) and ellipticity (0.2–0.3; Buote & Canizares 1994) of the X-ray gas in NGC 720 differ from those shown by

Table 6. PA and ellipticity for the GC systems of NGC 720, NGC 1023 and NGC 2768. The values for the GCs are determined by fitting equation (5) to the histograms of the azimuthal distribution. The table displays the values of the parameters for the total system, blue and red GCs along with the host galaxy stellar properties obtained from HyperLeda (Paturel et al. 2003).

	NGC 720				NGC 1023				NGC 2768		
	Type	PA (°)			Type	PA (°)			Type	PA (°)	
Galaxy	Stars	142 ± 5	0.47 ± 0.05	Galaxy	Stars	87 ± 5	0.58 ± 0.05	Galaxy	Stars	93 ± 3	0.60 ± 0.03
GCs	Total	138 ± 6	0.28 ± 0.06	GCs	Total	89 ± 7	0.35 ± 0.09	GCs	Total	89 ± 2	0.59 ± 0.03
GCs	Blue	142 ± 8	0.26 ± 0.06	GCs	Blue	110 ± 32	0.15 ± 0.15	GCs	Blue	90 ± 3	0.57 ± 0.04
GCs	Red	134 ± 6	0.37 ± 0.08	GCs	Red	84 ± 6	0.57 ± 0.08	GCs	Red	87 ± 3	0.60 ± 0.05

both the host galaxy stars and the total GC system. We note that the ellipticities of the X-ray gas and the blue subpopulation are in reasonable agreement. Although the ellipticities are consistent, we note that the PAs are not. This consistency in ellipticities implies that both the X-ray gas and blue subpopulation might have a common dynamical behaviour and hence strengthens the connection between the blue subpopulation and galaxy haloes (Forbes et al. 2012a).

3.6.2 NGC 1023

The azimuthal distribution for the NGC 1023 GCs is shown in Fig. 16. The profiles obtained from equation (5) are fitted to the different GC subpopulations and displayed in Fig. 16. The photometric PA for the galaxy NGC 1023 is 87° and the best fitted profile for the total and red GCs peaks at similar values within errors. The red GCs of NGC 1023 are aligned along the PA of the galaxy light with ellipticity, $= 0.57 \pm 0.08$. The best fitted profile generated by equation (5) for the blue GCs shows a flat distribution. The profile peaks at 110° ± 32° and represents a nearly circular distribution for the blue subpopulation of NGC 1023.

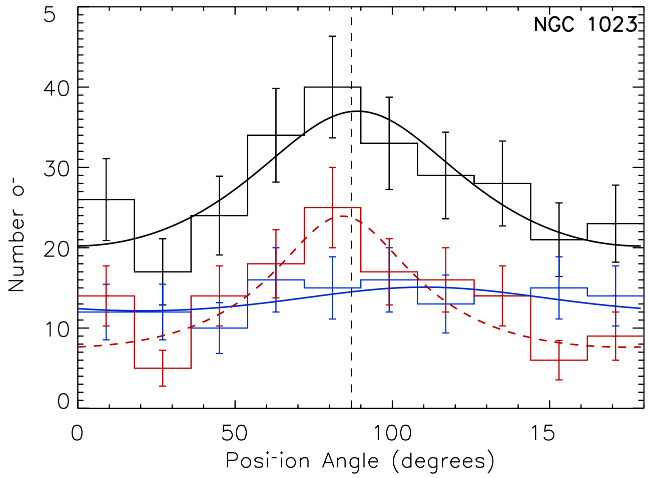

Figure 16. Azimuthal distribution of NGC 1023 GCs. The densities of total system of GCs and blue and red GC subpopulations are shown in black, blue and red histograms. The fitted lines (same patterns and colours as given in Fig. 15) represent the profile given by equation (5) for NGC 1023 GCs. The dashed vertical line represents the position angle of the galaxy light (PA = 87°). The total system and red subpopulation of NGC 1023 GCs are arranged in elliptical rings along the PA of the galaxy light. In contrast, the blue subpopulation shows a nearly flat azimuthal distribution (indicating a more circular distribution).

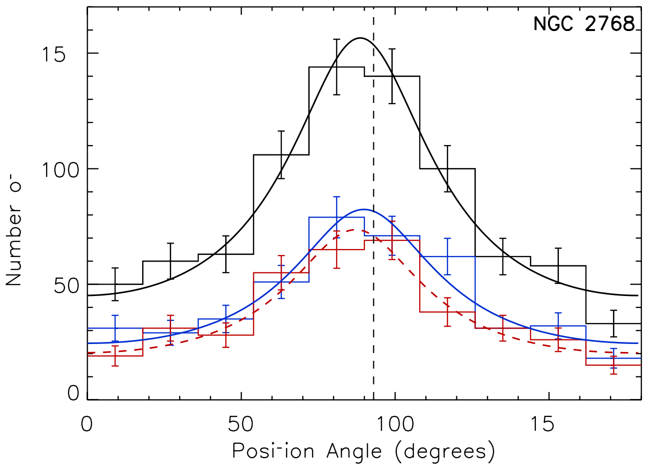

Figure 17. Azimuthal distribution of NGC 2768 GCs. The histograms in black, blue and red represent the azimuthal distribution of total, blue and red GCs of NGC 2768. The fitted lines (same patterns and colours as given in Fig. 15) represent the profile given by equation (5) for NGC 2768 GCs. The position angle of the galaxy stellar light (PA = 93°) is represented by the dashed vertical line. The total system, red and blue GCs of NGC 2768 have an ellipticity value of 0.58 ± 0.06. The PAs of the GC system and subpopulations match with the galaxy light of NGC 2768.

3.6.3 NGC 2768

Fig. 17 displays the azimuthal distribution of the total system, blue and red subpopulations of NGC 2768 GCs. The distributions are fitted with sinusoidal profiles given by equation (5) and are shown in this figure. Table 6 displays the PA and ellipticity values estimated from the fitted profiles. Both the blue and red GC subpopulations are distributed with ∼0.58 along the position angle of galaxy light (PA = 93°). In addition, the estimated values for the total GC system match well with both the subpopulations.

3.7 Specific frequency

Two key properties of a GC system that can be estimated accurately using wide-field imaging data are the total number of GCs and the specific frequency. The specific frequency (S_N) of a GC system is the total number of GCs in a galaxy per unit host galaxy luminosity. In order to compare the GC systems of galaxies, the value of S_N is a useful parameter. The value of S_N may be dependent on galaxy morphology, mass, luminosity and environment. For elliptical and lenticular galaxies, the value of S_N ranges from 2 to 6 (Harris 1991; Elmegreen 1999) depending on the host galaxy mass/luminosity.

The value of S_N is defined by the relation of Harris & van den Bergh (1981):

$$S_N = N_{\rm GC}\ 10^{0.4(M_V^T+15)}. \qquad (6)$$

The parameter $N_{\rm GC}$ (the total number of GCs) is estimated from the surface density distribution of GC systems. To determine the total number of GCs, the area under the Sérsic profile fitted to the radial density distribution of GCs (from the centre out to the radius at which it reaches the background) is integrated and then doubled (by assuming a symmetric GC luminosity function, only GCs within the turnover magnitude have been counted). M_V^T in equation (6) represents the total absolute magnitude in the V band.

For NGC 720, NGC 1023 and NGC 2768, the total number of GCs is estimated to be 1489 ± 96, 548 ± 59 and 744 ± 68, respectively. The total visual magnitude for the respective galaxies is $M_V^T = -21.68 \pm 0.05$, -21.07 ± 0.06 and -21.91 ± 0.1 mag. Hence, the specific frequency of GCs in NGC 720, NGC 1023 and NGC 2768 is calculated to be 3.2 ± 0.2, 1.8 ± 0.2 and 1.3 ± 0.1.

Kissler-Patig et al. (1996) estimated the total number of GCs for NGC 720 to be 660 ± 190. They derived a specific frequency of 2.2 ± 0.9. The GC extent used to derive these properties is 2.67 arcmin, but the extent from our study is 9.8 ± 0.8 arcmin. The difference in the estimation of GC extent is responsible for the difference in $N_{\rm GC}$ and hence S_N. For NGC 1023, Young et al. (2012) estimated $N_{\rm GC} = 490 \pm 30$ and $S_N = 1.7 \pm 0.3$ for the GC system of NGC 1023. With the estimation of a similar extent for GC system of NGC 1023, we have derived $N_{\rm GC} = 548 \pm 59$ and $S_N = 1.8 \pm 0.2$. Both the estimations are in good agreement with each other for NGC 1023. Kundu & Whitmore (2001) studied the GC system of NGC 2768 using *HST*/WFPC2 data and calculated the total number of GCs in their field of view as 343 with a local S_N of 1.2 ± 0.4 using $M_V^{\rm FOV} = -21.2$. The estimated $N_{\rm GC}$ using our wider field of view is double the number determined from the smaller field of view of WFPC2. We note that NGC 2768 is found to have a lower S_N value compared with S0 galaxies of similar luminosity (Brodie & Strader 2006).

4 GLOBAL RELATIONS OF GC SYSTEMS

In this section, we explore five global scaling relations between the GC systems and their host galaxy. Along with the above-discussed three galaxies, we include 33 literature studied galaxies plus four (NGC 821, NGC 1407, NGC 4278 and NGC 4365) galaxies from earlier SLUGGS studies. We have carried out a selection of galaxies based on their available GC system properties and used the same selection criteria as adopted in Spitler et al. (2008), followed from Rhode, Zepf & Santos (2005). The main criteria followed for the selection of literature galaxies are the GC system must have been observed in two filters with an estimate of total GC number, the fraction of blue to red GCs must have been given or can be calculated and the uncertainties in the estimated parameters should be <40 per cent. In our sample of 40 galaxies selected for this scaling relation study, three lack an estimate of GC system extent and the other two lack the ratio of blue to red GCs, but all have a reliable total GC number estimate.

4.1 GC system extent versus galaxy stellar mass

Rhode et al. (2007, 2010) have given a relation between the radial extent of a GC system and the host galaxy stellar mass for 11 galaxies. The extent of a GC system is defined as the radial distance at which the GC surface density distribution reaches the background. The host galaxy mass is estimated from the absolute visual magnitude making use of mass-to-light ratios given by Zepf & Ashman (1993). The mass-to-light ratios applied for the different Hubble types are as follows: $M/L = 10$ for elliptical galaxies, 7.6 for S0 galaxies, 6.1 for Sa–Sb galaxies and 5 for Sc galaxies. Before discussing the GC extent versus galaxy stellar mass relation, we discuss the possible sources of error.

The galaxy stellar mass is derived from the galaxy V-band magnitude, distance and mass-to-light ratio. Measurement of the total magnitude involves a typical error of 0.05–0.2 mag. Another large error comes from the mass-to-light ratio for different galaxy morphologies. For a given Hubble type, the mass-to-light ratio for a sample of galaxies is not constant. For example, NGC 1316 is included as an elliptical galaxy, and assumed to have a value of $M/L_V = 10$ (Zepf & Ashman 1993). However, Shaya et al. (1996) found a lower mass-to-light ratio of 2.2 for the galaxy. A possible explanation for the lower value is the presence of an intermediate-age stellar population (Shaya et al. 1996; Kuntschner 2000). Estimation of mass-to-light ratios for individual galaxies is a difficult process. Here we use the Zepf & Ashman (1993) values, but note the potentially large source of error.

Errors in the GC system extent include the galaxy distance errors, the bin size errors involved in GC surface density distribution and issues due to image quality. The main component determining a precise GC spatial extent is the imaging quality. In order to completely observe the extent of a GC system, wide-field imaging data from a large-aperture telescope must be used. Imaging data need to be observed in good seeing conditions which reduces the contamination in point source identification. Also GC selection from multifiltered imaging data reduces the contamination. For example, NGC 720 has a GC system three times larger (this work) than the literature estimate (Kissler-Patig et al. 1996), with the use of better quality and wider field data. The amount of contamination in a three-filter imaging data can be as low as ∼5 per cent (Romanowsky et al. 2009). Hence, accurate estimations of the GC system extent using wide-field imaging data is needed to reduce errors.

We have expanded the Rhode et al. (2007, 2010) studies of GC system extent versus host galaxy mass (for 11 galaxies) by including another 26 galaxies: 3 from this work, 4 from the earlier SLUGGS studies and 19 from other literature studies (as the GC system extent is not estimated for the other 3 galaxies). Table 7 tabulates the distance, total visual magnitude, estimated galaxy mass and the GC extent for the sample of 37 galaxies. The extent of GC systems against the host galaxy mass is plotted and displayed in Fig. 18. As the galaxy mass increases, it is evident from the figure that the extent of GC systems grows. Or in other words, more massive galaxies accommodate more extended GC systems.

The best fitted linear and second-order polynomials (not shown in Fig. 18) are

$$y = [(70.9 \pm 11.2) \times x] - (762 \pm 127) \qquad (7)$$

$$y = [(40.9 \pm 4.3) \times x^2] - [(879 \pm 97) \times x] + (4726 \pm 546), \qquad (8)$$

respectively, where x is the log stellar mass in $M_\odot$ and y is the spatial extent of the GC system in kpc. Fig. 18 also shows the linear fit from Rhode et al. (2007):

$$y = [(57.7 \pm 3.7) \times x] - (619 \pm 41). \qquad (9)$$

The slope of the linear fit has changed with the addition of more galaxies and is steeper than that in Rhode et al. (2007). The

Table 7. Properties of our galaxy sample. The top part of the table includes data for galaxies in the SLUGGS survey and the bottom part of the table lists other literature galaxies. Morphological type is taken from NED. The distances are obtained from Cappellari et al. (2011) if available, otherwise from NED. The total visual magnitude for the galaxies is taken from de Vaucouleurs et al. (1991) and hence we derive the absolute magnitude, M_V^T. The distance, absolute magnitude and the mass-to-light ratio (given by Zepf & Ashman 1993) are incorporated to determine the galaxy stellar mass (M_*). GC numbers ($N_{\rm GC}$) are taken from different references as recorded in the footnote. $N_{\rm BGC}/N_{\rm RGC}$ represents the ratio of blue to red GCs. The references corresponding to galaxy effective radii are also mentioned in the footnote. The local density parameter is taken from Tully (1988).

NGC	Type	D (Mpc)	V_T^0 (mag)	M_V^T (mag)	$\log(M_*)$ ($M_\odot$)	GCS ext. (kpc)	$N_{\rm GC}$	$N_{\rm BGC}/N_{\rm RGC}$	$R_{\rm e}$ (kpc)	ρ (Mpc^{-3})
720	E5	23.44	10.17	−21.68	11.604	68 ± 6	1584 ± 190[a]	1.85	4.60[w]	0.25
821	E6	23.40	10.79	−21.06	11.354	26 ± 3	320 ± 45[b]	2.33	4.51[x]	0.95
1023	S0	11.10	9.15	−21.07	11.243	20 ± 2	572 ± 94[a]	0.75	2.57[x]	0.57
1407	E0	23.11	9.74	−22.08	11.764	140 ± 7	6400 ± 700[c]	1.50	8.06[w]	0.42
2768	S0	21.80	9.78	−21.91	11.578	63 ± 3	714 ± 162[a]	2.33	6.66[x]	0.31
4278	E1	15.60	10.07	−20.90	11.290	64 ± 7	1700 ± 100[d]	1.78	2.39[x]	1.25
4365	E3	23.30	9.54	−22.30	11.851	134 ± 7	6450 ± 110[e]	1.63	5.92[x]	2.93
891	Sb	8.36	8.82	−20.79	11.034	9 ± 3	70 ± 20[f]	1.70	4.14[x]	0.55
1052	Sb	19.60	10.44	−21.02	11.341	19 ± 3	400 ± 120[g]	1.00	3.50[w]	1.80
1055	Sb	16.30	10.09	−20.97	11.106	26 ± 7	210 ± 40[h]	4.00	5.34[x]	0.25
1316	E	20.14	8.53	−22.99	11.526	62 ± 5	636 ± 35[i]	1.50	6.75[x]	1.15
1379	E0	17.71	10.99	−20.25	11.032	19 ± 2	225 ± 23[j]	0.82	3.64[w]	5.79
1387	S0	17.24	10.72	−20.46	10.998	14 ± 2	390 ± 27[j]	0.32	1.75[u]	5.80
1427	E3	19.35	10.91	−20.52	11.141	11 ± 2	470 ± 80[k]	4.56	3.08[w]	4.94
2683	Sb	7.70	8.97	−20.46	10.902	9 ± 3	120 ± 40[l]	2.03	2.10[x]	2.48
3258	E1	32.10	11.30	−21.23	11.425	–	6000 ± 150[m]	3.2	4.26[w]	0.72
3268	E2	34.80	11.30	−21.41	11.495	–	4750 ± 150[m]	1.6	6.08[w]	0.69
3379	E1	10.30	9.24	−20.82	11.262	34 ± 4	270 ± 68[n]	2.33	1.99[x]	4.12
3384	S0	11.30	9.84	−20.43	10.983	17 ± 4	120 ± 30[o]	1.50	1.77[x]	0.54
3556	Sb	7.10	9.26	−20.00	10.629	20 ± 4	290 ± 80[l]	1.70	3.00[x]	1.77
3585	E6	18.30	9.75	−21.56	11.557	36 ± 4	550 ± 55[p]	–	3.51[w]	0.12
4013	Sb	15.10	10.52	−20.37	10.867	14 ± 5	140 ± 20[f]	3.00	3.42[x]	1.34
4157	Sb	14.70	10.44	−20.40	10.876	21 ± 4	80 ± 20[l]	1.78	2.71[x]	7.55
4261	E2	30.80	10.39	−22.05	11.753	–	1242 ± 90[q]	1.50	5.67[x]	0.84
4374	E1	18.50	9.07	−22.27	11.838	30 ± 4	1775 ± 150[r]	2.33	4.70[x]	21.38
4406	E3	16.70	8.84	−22.27	11.841	83 ± 6	2900 ± 415[n]	1.50	7.55[x]	12.25
4472	E2	17.10	8.38	−22.78	12.046	102 ± 7	5900 ± 721[s]	1.50	7.91[x]	19.68
4594	Sa	9.80	7.55	−22.41	11.775	54 ± 5	1900 ± 189[n]	1.50	7.28[y]	0.95
4636	E0	14.30	9.51	−21.27	11.439	56 ± 5	4200 ± 120[t]	1.86	6.17[x]	9.44
4649	E2	17.30	8.75	−22.44	11.910	42 ± 3	3600 ± 500[u]	1.67	5.54[x]	3.49
4754	S0	16.10	10.43	−20.60	11.054	15 ± 4	115 ± 15[o]	0.67	2.47[x]	2.62
4762	S0	22.60	10.16	−21.61	11.457	27 ± 7	270 ± 30[o]	0.67	4.78[x]	2.65
5812	E0	27.95	10.89	−21.34	11.469	27 ± 3	400 ± 40[p]	–	3.23[w]	0.19
5813	E1	31.30	10.48	−22.00	11.731	120 ± 14	2900 ± 400[o]	2.13	8.73[x]	0.88
5866	S0	14.90	9.99	−20.88	11.163	44 ± 11	340 ± 80[o]	2.85	2.62[x]	0.24
7331	Sb	13.10	8.75	−21.84	11.452	18 ± 4	210 ± 130[l]	1.04	3.91[x]	1.59
7332	S0	23.00	11.06	−20.75	11.112	13 ± 4	175 ± 15[h]	4.00	1.94[x]	0.12
7339	Sbc	22.40	11.42	−20.33	10.850	10 ± 3	75 ± 10[h]	2.33	2.66[x]	0.11
7457	S0	13.20	10.93	−19.67	10.682	13 ± 2	210 ± 30[v]	1.50	2.32[x]	0.13
7814	Sb	17.17	10.20	−20.97	11.107	13 ± 4	190 ± 20[s]	0.67	3.39[x]	0.91

References : [a]This work, [b]Spitler et al. (2008), [c]Forbes et al. (2011), [d]Usher et al. (2013), [e]Blom et al. (2012), [f]Rhode et al. (2010), [g]Forbes, Georgakakis & Brodie (2001), [h]Young et al. (2012), [i]Richtler et al. (2012), [j]Bassino et al. (2006a), [k]Forte et al. (2001), [l]Rhode et al. (2007), [m]Bassino, Richtler & Dirsch (2008), [n]Rhode & Zepf (2004), [o]Hargis & Rhode (2012), [p]Lane, Salinas & Richtler (2013), [q]Bonfini et al. (2012), [r]Gómez & Richtler (2004), [s]Rhode & Zepf (2003), [t]Dirsch et al. (2005), [u]Lee et al. (2008), [v]Hargis et al. (2011), [w]Faber et al. (1989), [x]Cappellari et al. (2011), [y]Bender et al. (1992).

second-order polynomial fit given by equation (8) also provides a reasonable match to the data.

In order to better understand the relation between the GC system extent and host galaxy mass, we analysed the host galaxy's morphology. The total sample is divided into different Hubble types and shown with different symbols in the figure (see the caption of Fig. 18). Spiral galaxies are positioned at the bottom-left side of the figure. Since the extent of a GC system for spiral galaxies in the sample is found to be independent of the host galaxy mass, we did a separate analysis excluding them. In the total sample of galaxies, we have 17 elliptical galaxies and 10 lenticular galaxies. Although most of the early-type galaxies agree well with the fitted linear relation (within error bars), some are displaced from the fit (i.e. NGC 4365, NGC 1407, NGC 4374). Another linear fit is carried out only for the 27 early-type galaxies and is shown in Fig. 18, which is given by

$$y = [(80.5 \pm 15.7) \times x] - (872 \pm 179). \tag{10}$$

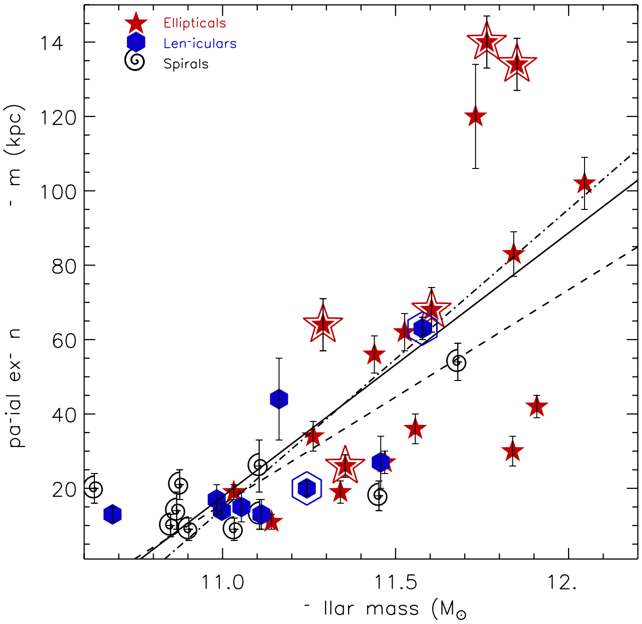

Figure 18. Radial extent of the GC system versus log galaxy mass. The galaxies studied by the SLUGGS survey are represented with double star and double hexagon symbols, while others represent galaxies studied using wide-field photometry from the literature. Elliptical, lenticular and spiral galaxies are drawn with star, hexagon and spiral symbols, respectively. The linear fits given by equations (7) and (10) are shown by a straight line and a dot–dashed line, respectively. The dashed line depicts the linear relation given by equation (9) from Rhode et al. (2007).

It is evident from Fig. 18 that the spatial extent of GC systems is larger for more luminous early-type galaxies.

With this limited sample of galaxies, we conclude that the spatial extent of GC systems is proportional to the host galaxy stellar mass. This result is in agreement with Rhode et al. (2007), but our linear fit is steeper than Rhode et al. (2007) (since the majority of their sample was spiral galaxies), when more galaxies are included. The main errors affecting the relation are the image quality and the assumed constant mass-to-light ratios for galaxies of individual Hubble type. With our sample of galaxies, we also infer that the extent of a GC system is only weakly dependent on the galaxy stellar mass for late-type galaxies.

4.2 GC extent versus galaxy effective radius

Given the errors associated with determining the galaxy stellar mass, we now examine the galaxy effective radius. The effective radius (R_e) is defined as the galaxy radius comprising half of the total luminosity. We exclude the late-type galaxies from this analysis because the effective radius for late-type galaxies includes the bulge plus extended disc components, but only the bulge component for early-type galaxies. This is done for the sake of uniformity.

The effective radii for early-type galaxies are taken from Faber et al. (1989), Bender, Burstein & Faber (1992) and Cappellari et al. (2011). The effective radius for NGC 1387 is taken from de Vaucouleurs et al. (1991) and we have multiple measurements for other galaxies. Faber et al. (1989) and Bender et al. (1992) estimated effective radii from de Vaucouleurs fits to the surface brightness profiles. Cappellari et al. (2011) derived the effective radii combining the RC3 and 2MASS determinations; both measurements are based on growth curves. Estimation of the effective radius includes a large error of ∼20 per cent (Cappellari et al. 2011). This error has a greater effect on larger sized galaxies (as shown in Fig. 19). The priority for effective radius values used here is Cappellari et al. (2011), then Faber et al. (1989) and finally Bender et al. (1992). The effective radii for the sample galaxies are also recorded in Table 7. Fig. 19 shows the GC system extent versus effective radius for early-type galaxies. As evident from the figure, the GC system extent is larger for greater effective radii. A linear fit is carried out for the sample of 27 galaxies and is represented with a straight line in Fig. 19. The fitted linear relation between the GC system size and galaxy size is given by

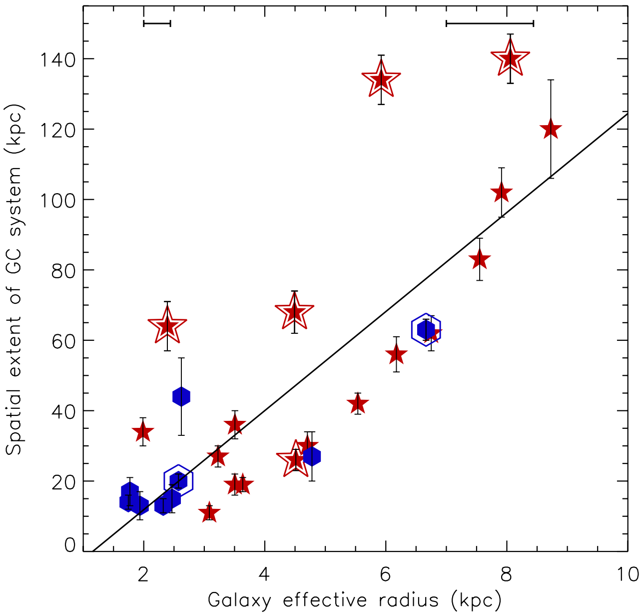

Figure 19. Radial extent of the GC system versus galaxy effective radius for early-type galaxies. The symbols shown in the figure are the same as in Fig. 18. The linear fit given by equation (11) is drawn with a solid line. The typical 20 per cent errors at $R_e = 2$ and 7 kpc are shown at the top of the figure.

$$y = [(14.1 \pm 2.1) \times x] - (16.2 \pm 10.1), \qquad (11)$$

where x represents the galaxy effective radius and y represents the spatial extent of the GC system. For a sample of 27 early-type galaxies, the extent of a GC system is ∼14 times the effective radius of the host galaxy. An advantage of this relation is that it is independent of an assumed mass-to-light ratio as needed in Section 4.1. Hence, Fig. 19 provides a better understanding between the GC system extent and their host galaxies.

4.3 GC system effective radius versus galaxy effective radius

Although we can confirm the correlation of the GC spatial extent with galaxy mass as found by Rhode et al. (2007), we also find evidence that the measurement of the spatial extent is strongly dependent on the quality of the data used. Thus, the Rhode et al. (2007) correlation should be considered more as a general trend than a quantitative relation. A better quantity to use is the effective radius of the GC system, although this has only been measured for a handful of GC systems to date.

Here we plot the GC system effective radius versus the galaxy effective radius. The effective radius of the GC system is derived from a Sérsic profile fitted to the radial GC surface density profile.

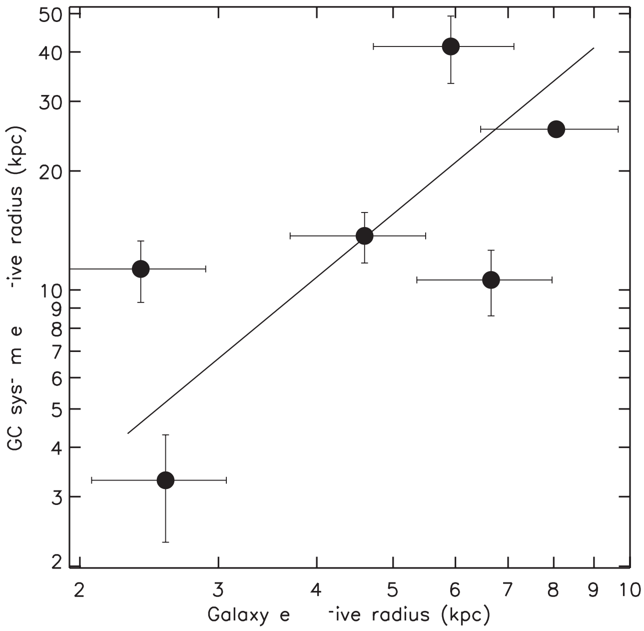

Figure 20. GC system effective radius versus galaxy effective radius. The plot displays six galaxies from the SLUGGS survey. The GC system effective radius is derived from the Sérsic profile fitted to the radial surface density distribution of GCs and the galaxy effective radius is discussed in Section 4.2. The straight line shown in the figure is given by fitting the data with the bootstrap technique.

Table 8. Effective radius of GC systems from a Sérsic fit and their host galaxy. The references for GC system and galaxy effective radii are given in the last column, respectively.

Galaxy NGC	Effective radius GC system (kpc)	Stellar light (kpc)	Ref.
720	13.7 ± 2.2	4.60 ± 0.9	1, 5
1023	3.3 ± 0.9	2.57 ± 0.5	1, 6
1407	25.5 ± 1.4	8.06 ± 1.6	2, 5
2768	10.6 ± 1.8	6.66 ± 1.3	1, 6
4278	11.3 ± 1.5	2.39 ± 0.5	3, 6
4365	41.3 ± 8.1	5.92 ± 1.2	4, 6

References: 1 – this work; 2 – Spitler et al. (2012); 3 – Usher et al. (2013); 4 – Blom et al. (2012); 5 – Faber et al. (1989); 6 – Cappellari et al. (2011).

Most literature studies have used a power law or de Vaucouleurs law (a Sérsic fit with n fixed to 4) to analyse the GC radial density distribution. Fig. 20 shows the plot for six SLUGGS galaxies available with both parameters (recorded in Table 8). We have linearly fitted the data with the bootstrap technique and found

$$y = [(5.2 \pm 3.7) \times x] - (8.5 \pm 6.5), \tag{12}$$

where x and y represent the galaxy and GC system effective radii, respectively.

The GC system spatial extent (shown in Figs 18 and 19) includes errors mainly from quality of data used. But the GC system effective radius is a more reliable parameter as it is derived from a Sérsic profile. Hence, we suggest the GC system effective radius versus galaxy effective radius as a better version of Fig. 18.

4.4 Ratio of blue to red GC number as a function of the host galaxy density

Tonini (2013) has performed a series of Monte Carlo simulations to study the assembly history of galaxies and the formation of associated GC systems. One prediction is that galaxies in higher density environments are expected to have a higher minor merger/accretion frequency and hence to contain a higher number of accreted blue GCs. According to Tonini's prediction, the ratio of blue to red GCs should be larger for galaxies in higher density environments.

To quantify the density of environment around a galaxy, we have employed the local density parameter. We use the local environment density as a proxy for the merger history in comparison with Tonini (2013). Tully (1988) has estimated the local density parameter ρ (in Mpc^{-3}) for 2367 galaxies in the Nearby Galaxies Catalog. He defined it as the number of galaxies per Mpc^{-3} found around a galaxy within a smoothing length σ. The density parameter is given by

$$\rho = \sum_i C \exp\,[-r_i^2/2\sigma^2], \tag{13}$$

where $C = 1/(2\pi\sigma^2)^{3/2} = 0.0635/\sigma^3$ is a normalization coefficient, r_i is the projected distance towards the ith galaxy from the central galaxy and the distribution around each galaxy is fitted with a Gaussian profile of half-width σ. The density parameter ρ is the sum over all galaxies excluding the central galaxy. The definition of ρ given above does not take into account the incompleteness of the catalogue at large distances. Hence, the ρ values calculated by Tully (1988) have a large uncertainty factor. The environmental measure should ideally give an indication of the merger/interaction history for individual galaxies. As such a measure is unavailable, we use ρ as a proxy.

Using our total sample of galaxies, we searched for confirmation of Tonini's prediction. The galaxies with reliable GC number ratios are selected based on the criteria mentioned in Section 4.1 and are tabulated in Table 7 along with ρ. Fig. 21 shows the ratio of blue to red GCs versus the local density parameter ρ. Galaxies of different morphological types are shown with different symbols in the figure. It is visible from the figure that there is no strong correlation between the density of environment and the blue-to-red GC number ratio for elliptical and spiral galaxies. However, we find an anticorrelation for the lenticular galaxies: the ratio of blue to red GCs decreases with increasing local density. With the bootstrapping technique, a best-fitting linear relation to the data points of lenticular galaxies is

$$y = [(-0.59 \pm 0.07) \times x] + (-0.031 \pm 0.052), \tag{14}$$

where x and y represent log(ρ) and log($N_{\mathrm{BGC}}/N_{\mathrm{RGC}}$), respectively. This negative slope implies that there is a higher relative number of red GCs for lenticular galaxies in denser environments. We note that the correlation still holds if the galaxy with the lowest blue-to-red ratio (NGC 1387) is removed from the sample.

Cho et al. (2012) studied 10 early-type galaxies in low-density environments using *HST*/ACS data. They compared the properties with cluster galaxies from the ACSVCS (Côté et al. 2004). They found that the mean colour of GCs is bluer and also the relative fraction of red GCs is lower for field galaxies than for the cluster galaxies from the ACSVCS. From these trends, they inferred that the galaxy environment has only a weak effect on the formation and mean metallicities of GCs, while the host galaxy luminosity/mass plays a major role. They also suggested a possible explanation for the environmental dependence whereby the GC formation in

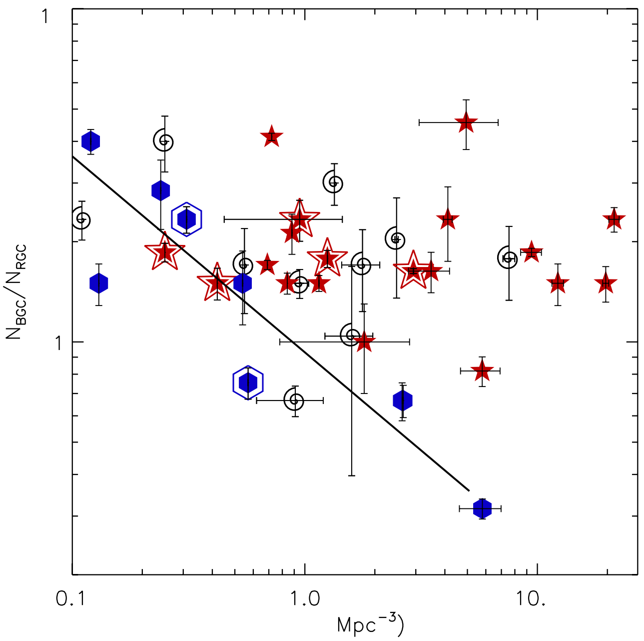

Figure 21. Ratio of blue to red GCs versus density of environment. Spiral, lenticular galaxies and elliptical galaxies are represented by spirals, hexagons and stars, respectively. The double symbol points represent the galaxies from the SLUGGS survey and others from the literature. We did not find any correlation for the spiral and elliptical galaxies. But we found that the ratio of blue to red GCs decreases with the density of environment for lenticular galaxies (the fitted linear relation is shown as a straight line). Note the presence of two overlapping galaxies, NGC 4754 and NGC 4762, around the coordinates (2.6, 0.7).

dense environments is affected by neighbouring galaxies through interaction/accretion which produces a large variation in the GC system properties for galaxies in high-density environments.

Spitler et al. (2008) investigated the relationships of $T_{\rm blue}$ (the number of blue GCs normalized to the host galaxy stellar mass) with host galaxy stellar mass (M_*) and local density ρ. They studied a sample of 25, mostly elliptical, galaxies with only two lenticular galaxies. Both $T_{\rm blue}$ versus M_* and $T_{\rm blue}$ versus ρ showed positive trends implying a lower $T_{\rm blue}$ value for lower mass galaxies and lower density environments. This supports the idea that the T parameter has a dependence on either mass or density or possibly both. Trying to disentangle the dependence, they noticed a slight positive trend in a residual plot of $T_{\rm blue}$ versus M_* after removing the dependence of $T_{\rm blue}$ on ρ. They argued that the GC formation efficiency is highly dependent on the host galaxy stellar mass, but much less so on the environmental density.

In our sample, the relative fraction of red GCs in lenticular galaxies increases with the environmental density (Fig. 21), while the same trend is not shown by elliptical or spiral galaxies. Cho et al. (2012) detected an increase in the relative fraction of red GCs with the environmental density. The majority of their galaxies are also lenticular galaxies, after combining with the ACSVCS data. Hence, our result matches with Cho et al. (2012). Thus, from our study, we also confirm the dependence of GC formation on the galaxy environment, at least for lenticular galaxies, as seen in Cho et al. (2012). However, Spitler et al. (2008) found that the GC formation is dependent on the host galaxy mass, and only weakly on the environmental density. Their result was based on a sample mostly of elliptical galaxies and does not show any environmental dependence. Similarly, the elliptical galaxies in our sample do not show any dependence on environment. Spiral galaxies in our sample also exhibit an independence of blue-to-red ratio from their environments.

We find a relatively higher fraction of red GCs in lenticular galaxies residing in high-density environments. Among the various galaxy interactions which can cause variations in GC numbers, as discussed in Forbes et al. (1997), is tidal stripping which removes the outer halo or blue GCs. For example, NGC 1387 is an S0 galaxy in our sample with the lowest relative fraction of blue to red GCs ($N_{\rm BGC}/N_{\rm RGC} = 0.32$). The lack of blue GCs could be caused by a tidal interaction between NGC 1387 and NGC 1399. Bassino et al. (2006a,b) observed a low number of blue GCs around NGC 1387 and an overabundance in the direction near to NGC 1399. They proposed this as a case of tidal stripping through which NGC 1399 has stripped away the outer halo of NGC 1387, creating a deficit of blue GCs compared to the red GCs. Using numerical simulations, Bekki et al. (2003) confirmed an asymmetry in the distribution of blue GCs around NGC 1399 and also suggested the influence of a tidal interaction with the nearby galaxies. We propose that the tidal stripping might be the cause for the observed trend by lenticular galaxies.

4.5 GC ellipticity versus galaxy stellar light ellipticity

Fig. 22 shows the relation between ellipticity for GC subpopulations and for galaxy stellar light. The ellipticity values of galaxy stellar light are derived by fitting ellipses on the radial light distribution, and the GC subpopulations are estimated from the azimuthal distribution of GCs. Most literature studies have examined the azimuthal distribution of the total GC system and not for individual GC subpopulations. Hence, we have accessible values for GC subpopulation ellipticity for only a handful of galaxies. Table 9 displays

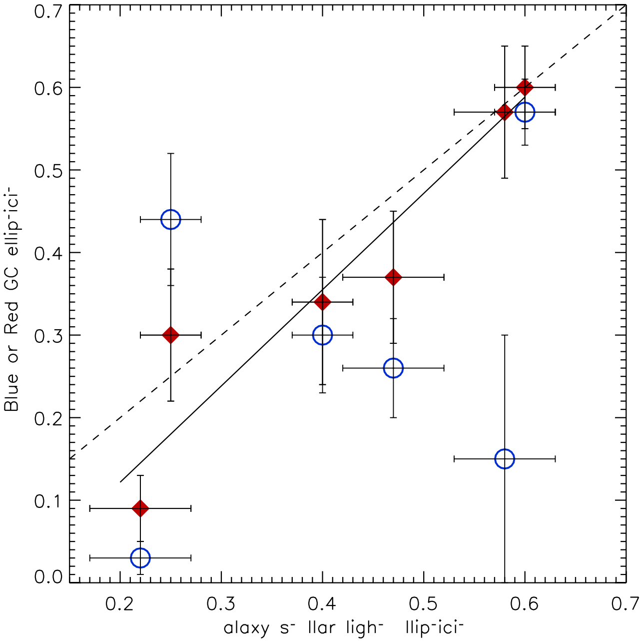

Figure 22. GC ellipticity versus galaxy stellar light ellipticity. The plot shows the relation between ellipticities of blue GCs or red GCs versus galaxy stellar light for six galaxies, recorded in Table 9. The blue and the red GCs are represented by blue open circles and red filled diamonds, respectively. A linear fit to the red GCs is drawn as a solid line and a one-to-one relation is shown as a dashed line.

Table 9. Ellipticity values for GC subpopulations and their respective galaxy stellar light for the six galaxies. The references for GCs and galaxy stellar light are given in the last column.

Galaxy NGC	Ellipticity Blue GCs	Ellipticity Red GCs	Ellipticity Stellar light	Ref.
720	0.26 ± 0.06	0.37 ± 0.08	0.47 ± 0.05	1, 5
1023	0.15 ± 0.15	0.57 ± 0.08	0.58 ± 0.05	1, 5
2768	0.57 ± 0.04	0.60 ± 0.05	0.60 ± 0.03	1, 5
4365	0.44 ± 0.08	0.30 ± 0.08	0.25 ± 0.03	2, 2
4486	0.30 ± 0.07	0.34 ± 0.10	0.40 ± 0.05	3, 3
4649	0.03 ± 0.02	0.09 ± 0.04	0.22 ± 0.05	4, 4

References: 1 – this work; 2 – Blom et al. (2012); 3 – Strader et al. (2011); 4 – Lee et al. (2008); 5 – Paturel et al. (2003).

the ellipticity values for blue and red GCs and the galaxy stellar light for six available galaxies.

We observe a positive correlation between the ellipticity for red GCs and galaxy stellar light (Fig. 22). But the distribution of blue GCs shows no trend. Using the bootstrap technique, we are able to fit a linear relation to the red GCs:

$$y = [(1.1 \pm 0.2) \times x] + (-0.1 \pm 0.1), \tag{15}$$

where x and y are ellipticities for galaxy stellar light and red GCs. This linear relation between the galaxy stellar light and red GCs is also consistent with the one-to-one relation, which is also drawn in Fig. 22. This suggests that both the red GC subpopulation and the underlying stellar populations share a common evolutionary history (see also Forbes et al. 2012a). This supports the GC formation scenarios which predict that the red GC subpopulation have originated along with the majority of galaxy stars. These scenarios suggested that the blue GC subpopulation formed before the red GCs.

Recently, Park & Lee (2013) studied the ellipticities of blue and red GC subpopulations and the host galaxy stellar light in 23 early-type galaxies using *HST*/ACSVCS. They found a tight correlation between the ellipticities of the red GC subpopulation and the galaxy stellar light, while a less tight trend for the blue GC subpopulation. Thus, their findings support our results from a smaller sample with wider field data.

5 CONCLUSIONS

We have carried out a detailed study of GC systems in three early-type galaxies: NGC 720, NGC 1023 and NGC 2768. The galaxies were observed in multiband wide-field images using the 8 m Subaru telescope, the 3.6 m CFHT and the 2.4 m *HST*. The main conclusions are discussed below.

(i) The spatial extent of the GC systems of NGC 720, NGC 1023 and NGC 2768 is estimated as 68 ± 6, 20 ± 2 and 63 ± 3 kpc, respectively. The spatial extent matches well with the literature for NGC 1023 and we provide a first estimate of the GC system extent for NGC 720 and NGC 2768.

(ii) The radial surface densities of GCs are fitted with Sérsic profiles. From the Sérsic fits, we estimated that the effective radii for the GC systems of NGC 720, NGC 1023 and NGC 2768 are 13.7 ± 2.2, 3.3 ± 0.9 and 10.6 ± 1.8 kpc, respectively.

(iii) CMDs show bimodal colour distributions of GCs in all three galaxies with greater than 99.99 per cent probability in all three galaxies.

(iv) The total number of GCs are estimated as 1489 ± 96, 548 ± 59 and 744 ± 68 for NGC 720, NGC 1023 and NGC 2768, respectively. The S_N values for the corresponding galaxies are 3.2 ± 0.2, 1.8 ± 0.2 and 1.3 ± 0.1.

(v) The peak colour of the blue and red GC subpopulations agrees with the GC colour–host galaxy luminosity relation (Peng et al. 2006; Faifer et al. 2011). This strengthens the fact that more massive galaxies have more metal enrichment.

(vi) The PA of the host galaxy matches with both the blue and red subpopulations in all three galaxies. Ellipticity values of the host galaxies match better with the red subpopulation than the blue subpopulation for all three galaxies.

We discuss five global relationships between the host galaxy and the GC system. We found that the spatial extent of a GC system is dependent on the host galaxy stellar mass/luminosity and the effective radius of the galaxy. Knowing the host galaxy luminosity, or the size of the galaxy, can therefore provide an estimation of the extent of the GC system. The extent of a GC system is determined to be ~14 times the effective radius of the host galaxy. The spatial extent of GC systems in elliptical and lenticular galaxies shows a strong dependence on the host galaxy stellar mass, but not for spiral galaxies.

We have analysed the relation between ellipticities for blue and red GC subpopulations and galaxy stellar light for a sample of six galaxies. The ellipticity for the red GC subpopulation appears to be correlated with the galaxy stellar light ellipticity for this sample. We support the view that the red GCs and the galaxy stellar light have a coeval formation. This result from a small sample of six galaxies is supported by Park & Lee (2013).

We have also found that the relative fraction of blue to red GCs decreases with galaxy environment density for lenticular galaxies. This result is in general agreement with the observations of Cho et al. (2012) and in disagreement with the predictions of Tonini (2013). We did not observe any specific trend for elliptical (supporting Spitler et al. 2008) and spiral galaxies with galaxy environment density. An interaction between galaxies, which can decrease the blue GC number in cluster environments, is tidal stripping. Through tidal effects, the outer halo (containing the blue GCs) of the small galaxy may have stripped away giving a lower fraction of blue to red GCs (Forbes et al. 1997; Bassino et al. 2006a,b) for lenticular galaxies in cluster environments.

ACKNOWLEDGEMENTS

We thank the anonymous referee for his/her careful reading of the manuscript and the valuable feedbacks. We also thank the members of SAGES group for the support and enlightening discussions. We thank N. Pastorello for the careful reading of the manuscript. We also acknowledge the useful comments from C. Tonini, C. Blom, C. Usher, V. Pota and N. Pastorello. With great pleasure we thank F. Faifer for providing us with the Gemini/GMOS data. SSK thanks the Swinburne University for the SUPRA fellowship. DAF thanks the ARC for support via DP-130100388. This research is supported in part by National Science Foundation grants AST-0909237 and AST-1211995. This paper was based in part on data collected at the Subaru telescope, which is operated by the National Astronomical Observatory of Japan. This paper uses data products produced by the OIR Telescope Data Center, supported by the Smithsonian Astrophysical Observatory. This work is based on observations made with the NASA/ESA *Hubble Space Telescope*, and obtained from the Hubble Legacy Archive, which is a collaboration between the Space Telescope Science Institute (STScI/NASA), the Space Telescope European Coordinating

Facility (ST-ECF/ESA) and the Canadian Astronomy Data Centre (CADC/NRC/CSA). This work is also based on observations obtained with MegaPrime/MegaCam, a joint project of CFHT and CEA/DAPNIA, at the Canada–France–Hawaii Telescope (CFHT) which is operated by the National Research Council (NRC) of Canada, the Institut National des Science de l'Univers of the Centre National de la Recherche Scientifique (CNRS) of France and the University of Hawaii. This research has made use of the NASA/IPAC Extragalactic Database (NED) operated by the Jet Propulsion Laboratory, California Institute of Technology, under contract with the National Aeronautics and Space Administration. We acknowledge the usage of the HyperLeda data base (http://leda.univ-lyon1.fr).

REFERENCES

Ashman K. M., Zepf S. E., 1992, ApJ, 384, 50
Ashman K. M., Bird C. M., Zepf S. E., 1994, AJ, 108, 2348
Bassino L. P., Richtler T., Dirsch B., 2006a, MNRAS, 367, 156
Bassino L. P., Faifer F. R., Forte J. C., Dirsch B., Richtler T., Geisler D., Schuberth Y., 2006b, A&A, 451, 789
Bassino L. P., Richtler T., Dirsch B., 2008, MNRAS, 386, 1145
Bekki K., Forbes D. A., Beasley M. A., Couch W. J., 2003, MNRAS, 344, 1334
Bender R., Burstein D., Faber S. M., 1992, ApJ, 399, 462
Bertin E., 2006, in Gabriel C., Arviset C., Ponz D., Enrique S., eds, ASP Conf. Ser. Vol. 351, Astronomical Data Analysis Software and Systems XV. Astron. Soc. Pac., San Francisco, p. 112
Bertin E., Arnouts S., 1996, A&AS, 117, 393
Bertin E., Mellier Y., Radovich M., Missonnier G., Didelon P., Morin B., 2002, in Bohlender D. A., Durand D., Handley T. H., eds, ASP Conf. Ser. Vol. 281, Astronomical Data Analysis Software and Systems XI. Astron. Soc. Pac., San Francisco, p. 228
Blom C., Spitler L. R., Forbes D. A., 2012, MNRAS, 420, 37
Bonfini P., Zezas A., Birkinshaw M., Worrall D. M., Fabbiano G., O'Sullivan E., Trinchieri G., Wolter A., 2012, MNRAS, 421, 2872
Boulade O. et al., 2003, in Iye M., Moorwood A. F. M., eds, Proc. SPIE Conf. Ser. Vol. 4841, Instrument Design and Performance for Optical/Infrared Ground-based Telescopes. SPIE, Bellingham, p. 72
Brodie J. P., Huchra J. P., 1991, ApJ, 379, 157
Brodie J. P., Strader J., 2006, ARA&A, 44, 193
Brodie J. P., Romanowsky A. J., Strader J., Forbes D. A., 2011, AJ, 142, 199
Brodie J. P., Usher C., Conroy C., Strader J., Arnold J. A., Forbes D. A., Romanowsky A. J., 2012, ApJ, 759, L33
Buote D. A., Canizares C. R., 1994, ApJ, 427, 86
Buote D. A., Canizares C. R., 1996, ApJ, 468, 184
Buote D. A., Canizares C. R., 1997, ApJ, 474, 650
Buote D. A., Jeltema T. E., Canizares C. R., Garmire G. P., 2002, ApJ, 577, 183
Capaccioli M., Lorenz H., Afanasjev V. L., 1986, A&A, 169, 54
Cappellari M. et al., 2011, MNRAS, 413, 813
Cho J., Sharples R. M., Blakeslee J. P., Zepf S. E., Kundu A., Kim H.-S., Yoon S.-J., 2012, MNRAS, 422, 3591
Cortesi A. et al., 2011, MNRAS, 414, 642
Côté P., Marzke R. O., West M. J., 1998, ApJ, 501, 554
Côté P., Marzke R. O., West M. J., Minniti D., 2000, ApJ, 533, 869
Côté P., West M. J., Marzke R. O., 2002, ApJ, 567, 853
Côté P. et al., 2004, ApJS, 153, 223
Crocker A. F., Bureau M., Young L. M., Combes F., 2008, MNRAS, 386, 1811
de Vaucouleurs G., de Vaucouleurs A., Corwin H. G., Jr, Buta R. J., Paturel G., Fouqué P., 1991, Third Reference Catalogue of Bright Galaxies. Volume I: Explanations and references. Volume II: Data for galaxies between 0^h and 12^h. Volume III: Data for galaxies between 12^h and 24^h. Springer-Verlag, Berlin
Dirsch B., Schuberth Y., Richtler T., 2005, A&A, 433, 43
Elmegreen B. G., 1999, Ap&SS, 269, 469
Faber S. M., Wegner G., Burstein D., Davies R. L., Dressler A., Lynden-Bell D., Terlevich R. J., 1989, ApJS, 69, 763
Faifer F. R. et al., 2011, MNRAS, 416, 155
Forbes D. A., Franx M., Illingworth G. D., Carollo C. M., 1996, ApJ, 467, 126
Forbes D. A., Brodie J. P., Grillmair C. J., 1997, AJ, 113, 1652
Forbes D. A., Georgakakis A. E., Brodie J. P., 2001, MNRAS, 325, 1431
Forbes D. A., Spitler L. R., Strader J., Romanowsky A. J., Brodie J. P., Foster C., 2011, MNRAS, 413, 2943
Forbes D. A., Ponman T., O'Sullivan E., 2012a, MNRAS, 425, 66
Forbes D. A. et al., 2012b, MNRAS, 426, 975
Forte J. C., Geisler D., Ostrov P. G., Piatti A. E., Gieren W., 2001, AJ, 121, 1992
Forte J. C., Vega E. I., Faifer F., 2012, MNRAS, 421, 635
Gómez M., Richtler T., 2004, A&A, 415, 499
Gómez M., Richtler T., Infante L., Drenkhahn G., 2001, A&A, 371, 875
Gwyn S. D. J., 2008, PASP, 120, 212
Hargis J. R., Rhode K. L., 2012, AJ, 144, 164
Hargis J. R., Rhode K. L., Strader J., Brodie J. P., 2011, ApJ, 738, 113
Harris W. E., 1991, ARA&A, 29, 543
Harris W. E., 2009a, ApJ, 699, 254
Harris W. E., 2009b, ApJ, 703, 939
Harris W. E., van den Bergh S., 1981, AJ, 86, 1627
Hook I. M., Jørgensen I., Allington-Smith J. R., Davies R. L., Metcalfe N., Murowinski R. G., Crampton D., 2004, PASP, 116, 425
Jordi K., Grebel E. K., Ammon K., 2006, A&A, 460, 339
Kissler-Patig M., Richtler T., Hilker M., 1996, A&A, 308, 704
Kron R. G., 1980, ApJS, 43, 305
Kundu A., Whitmore B. C., 2001, AJ, 122, 1251
Kuntschner H., 2000, MNRAS, 315, 184
Lane R. R., Salinas R., Richtler T., 2013, A&A, 549, A148
Larsen S. S., Brodie J. P., 2000, AJ, 120, 2938
Lee M. G., Park H. S., Kim E., Hwang H. S., Kim S. C., Geisler D., 2008, ApJ, 682, 135
Liu C., Peng E. W., Jordán A., Ferrarese L., Blakeslee J. P., Côté P., Mei S., 2011, ApJ, 728, 116
McLaughlin D. E., Harris W. E., Hanes D. A., 1994, ApJ, 422, 486
Miyazaki S. et al., 2002, PASJ, 54, 833
Muratov A. L., Gnedin O. Y., 2010, ApJ, 718, 1266
Ouchi M. et al., 2004, ApJ, 611, 660
Park H. S., Lee M. G., 2013, ApJ, 773, L27
Paturel G., Petit C., Prugniel P., Theureau G., Rousseau J., Brouty M., Dubois P., Cambrésy L., 2003, A&A, 412, 45
Peng E. W. et al., 2006, ApJ, 639, 95
Peng E. W. et al., 2008, ApJ, 681, 197
Pota V. et al., 2013, MNRAS, 428, 389
Rhode K. L., Zepf S. E., 2003, AJ, 126, 2307
Rhode K. L., Zepf S. E., 2004, AJ, 127, 302
Rhode K. L., Zepf S. E., Santos M. R., 2005, ApJ, 630, L21
Rhode K. L., Zepf S. E., Kundu A., Larner A. N., 2007, AJ, 134, 1403
Rhode K. L., Windschitl J. L., Young M. D., 2010, AJ, 140, 430
Richtler T., Bassino L. P., Dirsch B., Kumar B., 2012, A&A, 543, A131
Romanowsky A. J., Strader J., Spitler L. R., Johnson R., Brodie J. P., Forbes D. A., Ponman T., 2009, AJ, 137, 4956
Sancisi R., van Woerden H., Davies R. D., Hart L., 1984, MNRAS, 210, 497
Sandage A., Bedke J., 1994, The Carnegie Atlas of Galaxies. Volumes I, II. Carnegie Institution of Washington, Washington, DC
Schlegel D. J., Finkbeiner D. P., Davis M., 1998, ApJ, 500, 525
Shaya E. J. et al., 1996, AJ, 111, 2212
Sinnott B., Hou A., Anderson R., Harris W. E., Woodley K. A., 2010, AJ, 140, 2101
Spitler L. R., Forbes D. A., Strader J., Brodie J. P., Gallagher J. S., 2008, MNRAS, 385, 361
Spitler L. R., Romanowsky A. J., Diemand J., Strader J., Forbes D. A., Moore B., Brodie J. P., 2012, MNRAS, 423, 2177

Strader J. et al., 2011, ApJS, 197, 33
Tonini C., 2013, ApJ, 762, 39
Tully R. B., 1988, Nearby Galaxies Catalog. Cambridge Univ. Press, Cambridge
Usher C. et al., 2012, MNRAS, 426, 1475
Usher C., Forbes D. A., Spitler L. R., Brodie J. P., Romanowsky A. J., Strader J., Woodley K. A., 2013, MNRAS, preprint (arXiv:1308.6585)
Wang Q., Peng E. W., Blakeslee J. P., Côté P., Ferrarese L., Jordán A., Mei S., West M. J., 2013, ApJ, 769, 145
Young M. D., Dowell J. L., Rhode K. L., 2012, AJ, 144, 103
Zepf S. E., Ashman K. M., 1993, MNRAS, 264, 611

This paper has been typeset from a TEX/LATEX file prepared by the author.